ELSEVIER

Catalysis Today 23 (1995) 161–199

CATALYSIS
TODAY

Electron microscopy of catalysts; the present, the future and the hopes

Miguel José-Yacamán, Gabriela Díaz, Alfredo Gómez

Instituto de Física, Universidad Nacional Autónoma de México, Apartado Postal 20-364, Delegación Alvaro Obregón, 01000 México, D.F., Mexico

1. Introduction, where do we stand?

Any deep understanding of the science of catalytic phenomena implies a knowledge of the atomic structure of the catalyst. Whether it is a small metal particle, a sulphide or an oxide there is a great need to learn about the nature of the active sites. Transmission electron microscopy (TEM) appears intuitively to be a most suited technique to obtain information about the details of the structure. Its large spatial resolution and ability of correlate diffraction information with images are ideal for working out a structure. Nevertheless TEM has been often met with frustration by the catalytic community. For instance Che and Bennet [1] state the problem; ''often an article presents micrographs with black, grey and light blobs that are claimed by the authors to represent metal and support particles. How this is known is sometimes not clear''. We believe that this statement is true. Many times we can find in the literature TEM work which is done without the proper insight into the technique. It is clear that TEM is not a technique in which you put the sample, push a button and then obtain a number. A useful picture requires a lot of work and most often the expertise of a fully trained scientist.

The technique however has changed dramatically over the years. Most of the work using TEM done in the decade of the mid-60's to the mid-70's [2–4] assumed that the contrast of a small particle was due basically to 'mass thickness' contrast; the same way that a biological sample produces contrast. The assumption behind this idea was that a small particle had an amorphous structure. In fact the authors remember a colourful discussion back in 1974 in which a then well-known researcher stated ''the small particles never heard about the Bragg law''. This remark clearly shows the conservative concept that prevented TEM making any impact on the field for many years.

In the mid-70's theoretical evidence clearly pointed out that the nanometer particles were not structureless [5]. A quantum leap was produced in TEM of catalysts by the recognition of the crystalline nature of the particles. A number of medium resolution techniques of the mid-70's to the mid-80's produced useful information about the samples. Typical techniques were the weak-beam dark field technique [6], micro-diffraction studies [7,8], selected zone dark field studies [9] and other techniques that changed very quickly the landscape. For a review of these techniques see José-Yacamán and Avalos Borja [10]. A lot was learnt about the shape of particles. For instance in the case of Pt–graphite systems the cubo-octahedral shape was found [11]. Probably the most interesting case was that of the icosahedral and decahedral shaped particles [12,13], whose nature was clearly shown by dark field tech-

0920-5861/95/$09.50
SSDI 0920-5861(94)00163-4

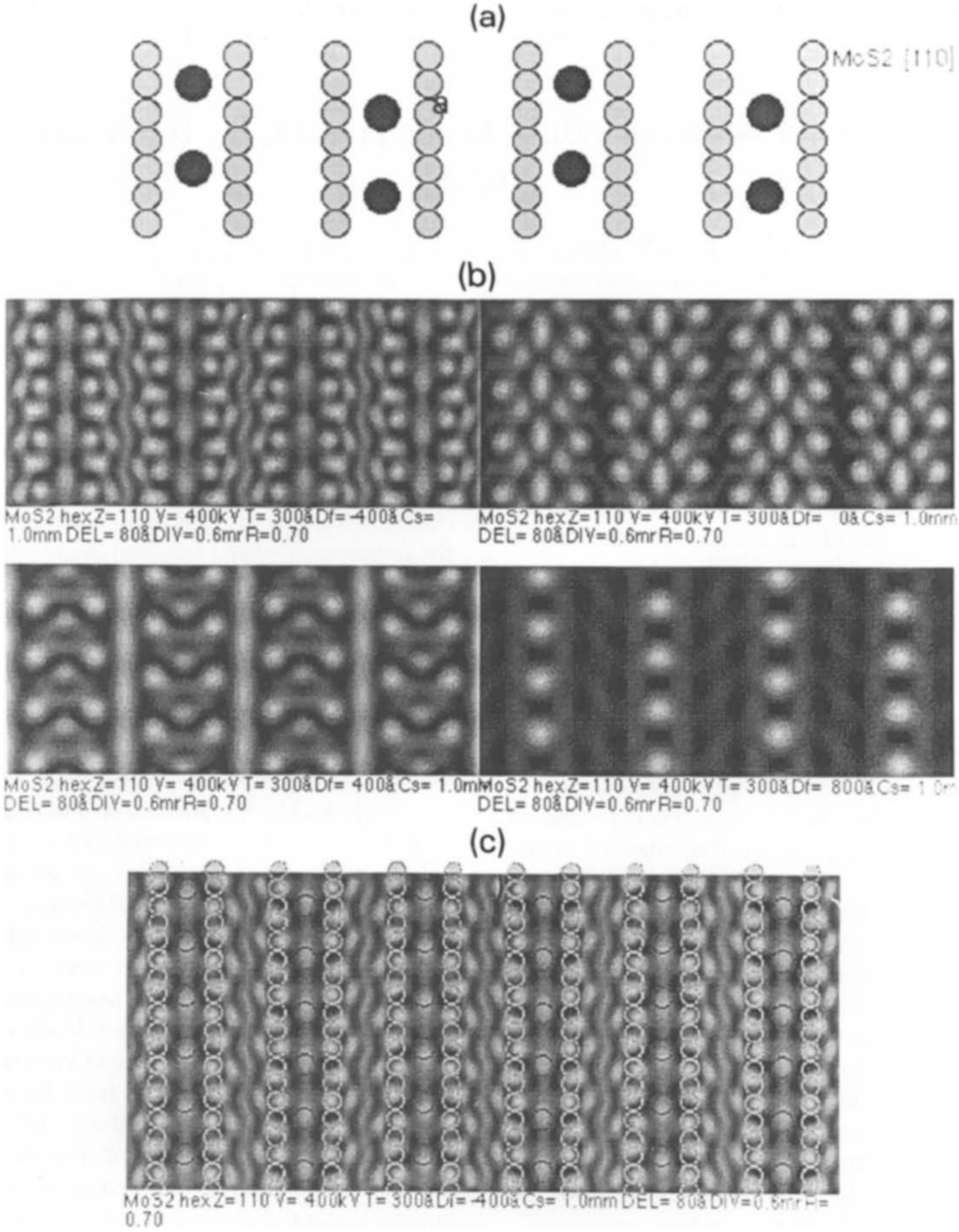

Fig. 1. Calculated image of a MoS_2 crystal on a $\langle 110 \rangle$ orientation. (a) Real sulphur atoms are small dots and large dots are Mo atoms. (b) Set of images obtained at different defocus conditions. (c) Superposition of an image obtained a $\Delta f = -400$ Å defocus and the real atomic positions (white dots). Note that the image has features which are not correlated to the structure.

niques. The fact that these particles are not single crystals and are formed by twin units immediately raised the question of whether the units follow the 'bulk' FCC structure (with homogeneous strain) or whether they change to a different structure (inhomogeneous strain). This controversy [14,15] ended when it became clear that both theories yield identical results (in images and diffraction patterns).

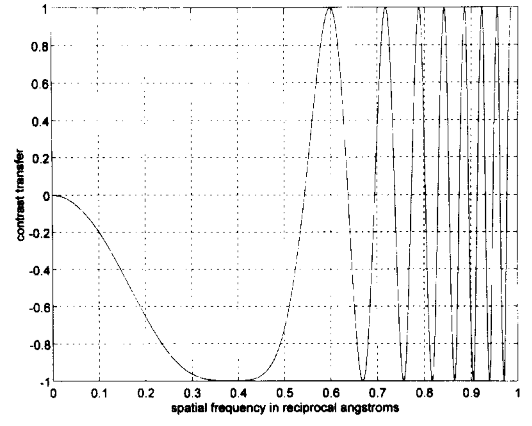

Fig. 2. Plot of the function $\sin(u,v)$ vs. the spatial frequency. This curve was obtained for the Scherzer defocus condition.

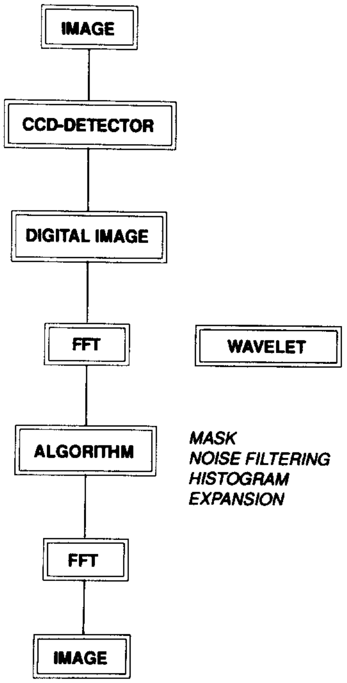

Fig. 3. Schematic representation of the steps involved in image processing.

In the 80's high-resolution electron microscopy entered the stage. There were immediately important results that came out from this technique such as steps in twin boundaries in large particles [10] and surface reconstruction in small particles [16]. However high-resolution microscopy produced a paradox. On the one hand manufacturers produced instruments with a very low spherical aberration coefficient C_s ca. 1.0 mm and a resolution of $d \approx 1.6$ Å point to point could be achieved at 400 keV with no great difficulty (leaving the old high-voltage machines obsolete). Unfortunately, on the other hand the gain in resolution brought a loss in interpretability. An example of the problem is shown in Fig. 1. The high-resolution image of a MoS_2 catalyst has been calculated using different defocus and objective aperture radius. The variations on the image are striking. This shows clearly that the interpretation of the images requires a lot of extra computational work. A single picture might not necessarily provide the proper information. Computer calculations are nowadays as necessary as the microscope itself.

The 90's have seen the emergence of image processing methods that are the current trend in the study of particles. It will be shown in this paper that image processing can produce the new quantum leap to particle characterisation. A standard criticism to TEM has been the problem of to what extent the observations are typical of the samples. Unlike X-ray diffraction, adsorption or activity measurements that give an average over the whole sample, TEM provides local information. After all, at the magnifications that can be achieved in modern microscopes, a modest sample of 1 cm^2 size amplified 10^6 times will have a size of 100 km^2 (probably the size of Mexico City or Tokyo). Therefore the issue of averaging over a large area of the sample becomes impossible even with a computer averaging a large number of images. Therefore the TEM has to be combined always with other techniques in order to obtain a complete characterisation of the sample.

In the present work we will discuss some of the high-resolution and image processing techniques and their use in catalyst characterisation. Several

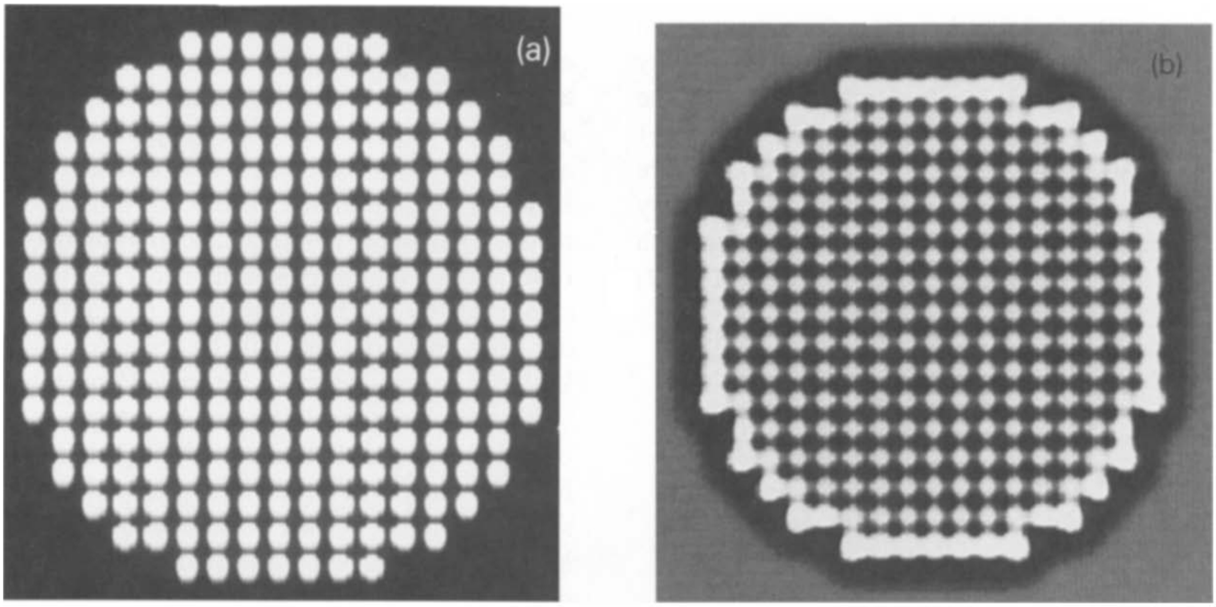

Fig. 4. (a) A theoretical small particle simulated by a computer. (b) The image filtered with a wavelet transform. Notice how the external shape of the particle is emphasised.

examples of practical applications will be presented.

2. Basic theory of image formation

The actual image observed on the screen or on the photographic plate is the result of two basic processes:

- The interaction of the electron beam with the sample. The electron beam, represented by an incoming wave function ψ_i impinges on the sample and as a result of its interaction with the atomic potential becomes ψ_o, the outgoing wave function.
- The interaction of the outgoing wave function with the microscope. Ideally the microscope should do nothing but produce an enlarged image of the potential distribution in the sample; in practice, microscopes are aberrated optical systems in which defocus, astigmatism, spherical aberration and chromatic aberration are present.

2.1. Interaction of the electron beam with the sample

First, some basic terminology. In what follows the potential that the electrons see will be represented by the function:

$$V(\vec{r}) = V(x,y,z)$$

It can be shown that the interaction of the electron beam with the sample can be described by dividing the sample into several slices, each of thickness Δz (here z is the coordinate in the direction of the incoming electron beam). The potential is considered as concentrated on the exit surface of each slice so the motion of the beam through the slice actually consists of two stages:

- Propagation from the entrance surface of the slice to the exit surface. Here the potential is considered to be zero (free particle propagation).
- Transmission by the potential (assumed to be concentrated at the exit surface).

So in a given slice, extending from z to $z+\Delta z$ the incoming wave function ψ_i (x,y,z) first becomes:

$$\psi_i^-(x,y,z+\Delta z) = \psi_i(x,y,z) * P_{\Delta z}(x,y)$$

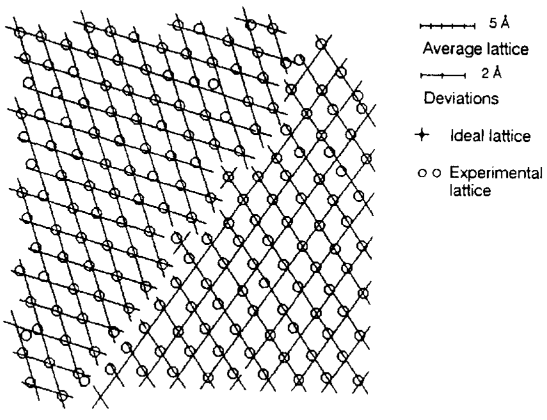

Fig. 5. Experimental reconstruction of the image of a catalyst with a boundary. The average lattices and the deviations of the atomic columns with respect to the average lattice are shown (greatly exaggerated). See text for explanation of the legend.

where the function

$$P_{\Delta z}(x,y) = \frac{-ie^{2\pi i\chi z}e^{i\pi(x^2+y^2)/\lambda\Delta z}}{\lambda z}$$

is the free space propagator as described in elementary textbooks on quantum mechanics. The various constants have their usual meaning; λ is the electron wavelength, $\chi = 1/\lambda$, $*$ denotes the convolution product. The $-$ in ψ_i^- is used to mean the wave function before transmission by the atomic potential.

The wave function Ψ_o $(x,y,z+\Delta z)$ exiting the slice is given by

$$\psi_o(x,y,z+\Delta z) = \psi_i^-(x,y,z+\Delta z)\ e^{-i\sigma V_p(x,y)}$$

where σ is the so-called interaction constant defined as

$$\sigma = \frac{\pi}{\lambda E}$$

with E being, in turn, the energy of the electrons. The function $V_p(x,y)$ is the projected potential of the slice

$$V_p(x,y) = \int_z^{z+\Delta z} V(x,y,z)\ dz$$

Putting the various pieces together

$$\psi_o(x,y,z+\Delta z) = (\psi_i(x,y,z) * P_{\Delta z}(x,y))\ e^{-i\sigma V_p(x,y)}$$

Once this is done for the first slice $\psi_o(x,y,z+\Delta z)$ is considered as the input wave function for the second slice

$$\psi_i(x,y,z+\Delta z) = \psi_o(x,y,z+\Delta z)$$

and the procedure is repeated for all the slices.

2.1.1. Weak phase object approximation

Frequently the potential term in $e^{-i\sigma V_p(x,y)}$ is sufficiently small that the so-called weak phase object approximation

$$e^{-i\sigma V_p(x,y)} \approx 1 - i\sigma V_p(x,y)$$

can be made.

2.2. Interaction of the electron beam with the microscope

There is a relationship between the wave function $\psi(x,y)$ leaving the sample and the wave function after the various lenses, mainly the objective lens. This relationship is expressed in reciprocal space (i.e. in terms of the Fourier transform of $\psi(x,y)$) as

$$\hat{\Psi}_m(u,v) = \hat{\Psi}(u,v)T(u,v)$$

where the $\hat{\Psi}_m$ represents the Fourier transform of the wave function after the lenses and $\hat{\Psi}$ represents the Fourier transform of the wave function before the lenses. The variables u and v are spatial frequencies and $T(u,v)$ is a function that describes the effect of the microscope and is called the contrast transfer function; it is given by:

$$T(u,v) = A(u,v)\, e^{i\chi(u,v)}$$

where

$$\chi(u,v) = \pi\lambda\left[D|(u,v)|^2 - \frac{1}{2}C_s\lambda^2|(u,v)|^4\right]$$

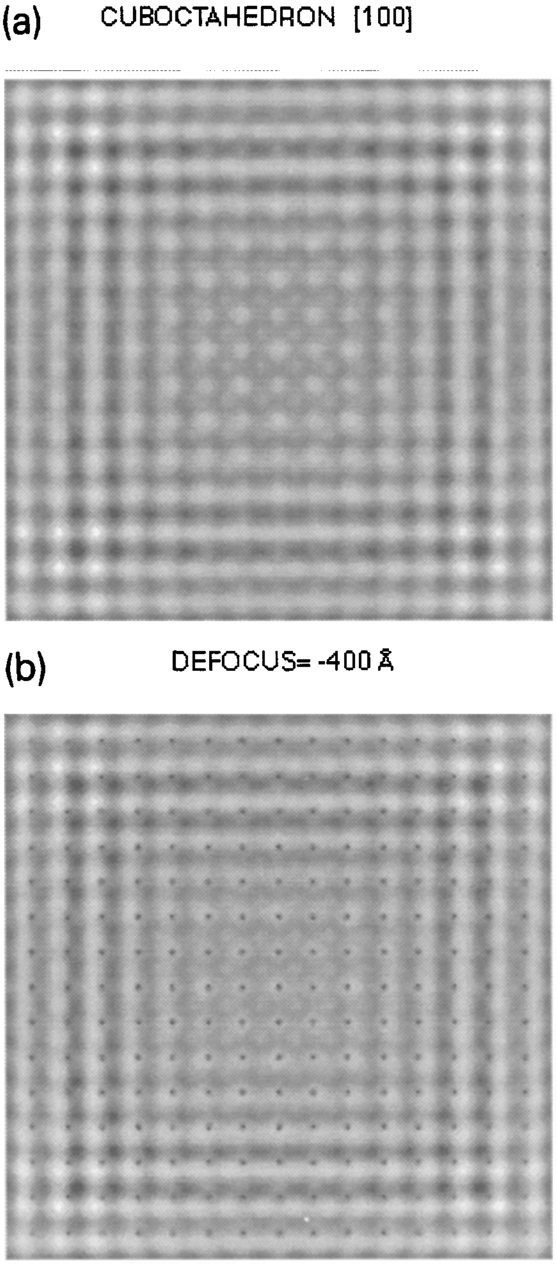

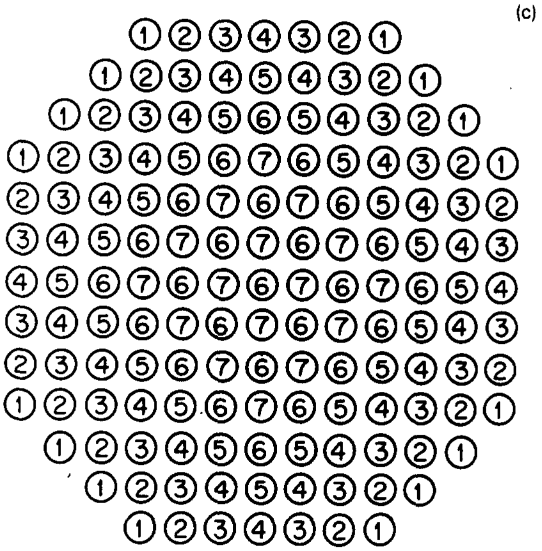

Fig. 6. (a) Calculated image of a cubo-octahedral particle with the ⟨100⟩ orientation. (b) The same image with the real atomic positions superimposed as black dots. (c) In the cubo-octahedral structure the columns contain a different number of atoms as indicated on the drawing.

Here D is the defocus and C_s is the spherical aberration coefficient.

2.2.1. *Weak phase object contrast*

Under the weak beam phase object approximation, when the transfer by the microscope is taken into account, the wave function becomes

$$\hat{\Psi}_m(u,v) = \hat{\Psi}(u,v)T(u,v)$$

$$= (\delta(u,v) - i\sigma\hat{V}_p(u,v))A(u,v)\, e^{i\chi(u,v)}$$

The intensity distribution at the image I can be calculated as $I = |\psi(x,y)|^2$ or better, in Fourier space as

$$\hat{I}(u,v) = \hat{\Psi}_m(u,v) * \hat{\Psi}^*_m(-u,-v)$$

It is more convenient to work not with I directly but instead with the contrast

$$c(x,y) = I(x,y) - 1$$

so from the previous equations

$$\hat{c}(u,v) = -2i\sigma\hat{V}_p(u,v)A(u,v)\ \mathrm{siny}(\chi)$$

This is probably the most important and useful equation when it comes to understand the relationship between what one sees and the structure

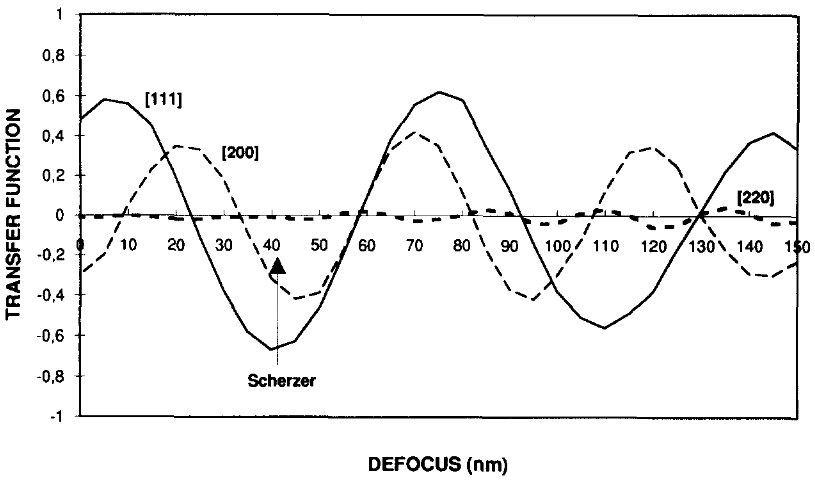

Fig. 7. Plot of the contrast transfer function vs. objective lens defocus obtained for the case of (111), (200) and (220) planes of gold.

of the sample. The part sin $(\chi(u,v))$ tells you how well the various spatial frequencies are transferred by the microscope. In Fig. 2 a plot of $\sin(\chi)$ is presented for the case of the so-called Scherzer defocus, a situation in which

$$D=\sqrt{C_s\lambda}$$

and the transfer is close to one for a broad range of frequencies. In this widely used defocus setting, atoms appear as dark dots. An extensive discussion of high-resolution methods can be found in the book by Spence [17].

3. Basis of image processing

Although there are many techniques for the digital image processing of micrographs, most of those relevant to the structural study of nanoparticulate catalysts are based in one way or another on a form of filtering.

If the density in a micrograph is given by a non-negative function $I(x,y)$ (or its discrete analogue), its Fourier transform is given by

$$\hat{I}(u,v)=\int_{-\infty}^{\infty} I(x,y)\ \mathrm{e}^{-2\pi i(ux+vy)}\ \mathrm{d}x\,\mathrm{d}y$$

and can be computed numerically by sampling I and using fast Fourier transform techniques. The commonest form of filtering involves a mask, that is a function S that has as values

$$S(u,v)=\begin{cases}1 \text{ for } (u,v) \in \text{ a given region } R\\ 0 \text{ for } (u,v) \text{ outside } R\end{cases}$$

Many different filtering functions can be used.

The process of filtering is accomplished by multiplying first $I(u,v)$ by $S(u,v)$ and then transforming back (inverse Fourier transform) so the filtered image $I'(x,y)$ is given by

$$I'(x,y)=F^{-1}[\hat{I}(u,v)S(u,v)]$$

where F^{-1} stands for the inverse Fourier transform.

In practical terms the processing involves several steps:

- The electron micrograph is digitised, i.e. it is sampled and the values of the density of the micrograph are stored in a matrix $I_{i,j}$ where the indices i and j run from 1 to the number of samples in each direction.
- The digitised image is Fourier transformed using the discrete version of the Fourier transform

  $$\hat{I}(i,j)=\sum_{h,k} I_{i,j}\,\mathrm{e}^{-2\pi i(hi+kj)}$$

  and taking advantage of the so-called Fast Fourier Transform algorithms.
- The masks for filtering are designed. They are devised in such a way that some specific spatial frequencies are obstructed (a sort of digital

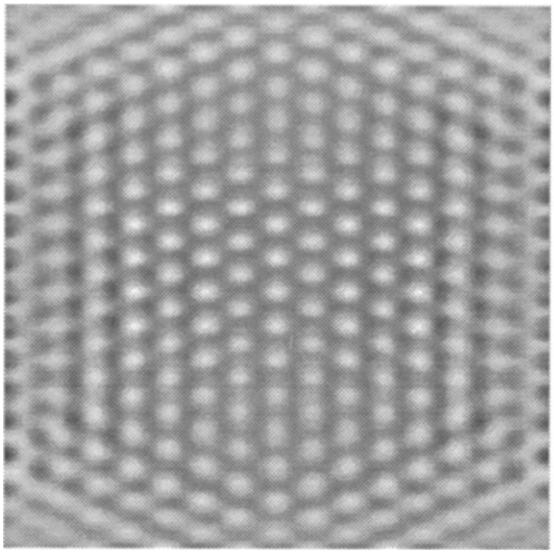

Pt Z=110 V=400 KeV Df=-400 Å Cs=1.0 mm

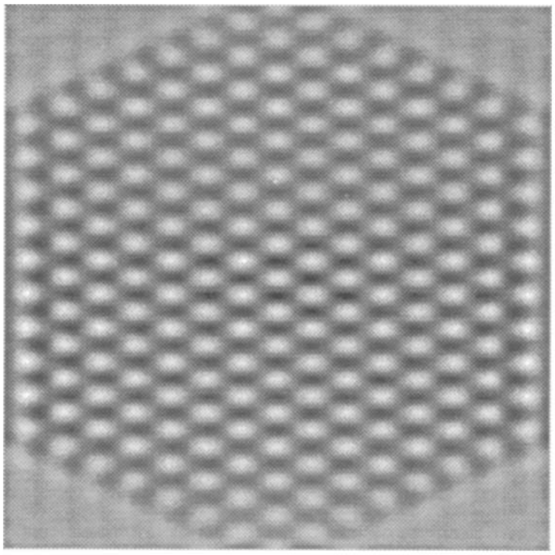

Pt Z=110 V=400 KeV Df=700 Å Cs=1.0 mm

Fig. 8. Theoretically calculated images of a gold cubo-octahedral with 2057 atoms particle calculated using a N-beam diffraction software. The particle has a ⟨110⟩ orientation and it is shown at different defocus conditions.

dark field). Another frequent case is that in which the highest spatial frequencies (those associated with noise) are removed. Other algorithms include contrast streaking, histogram expansion and several other. In a final

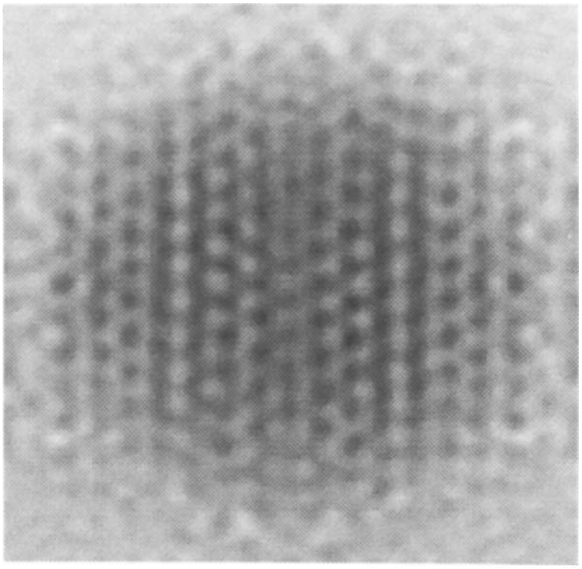

Pt Z=111 V=400 KeV Df=-400 Å Cs=1.0 mm

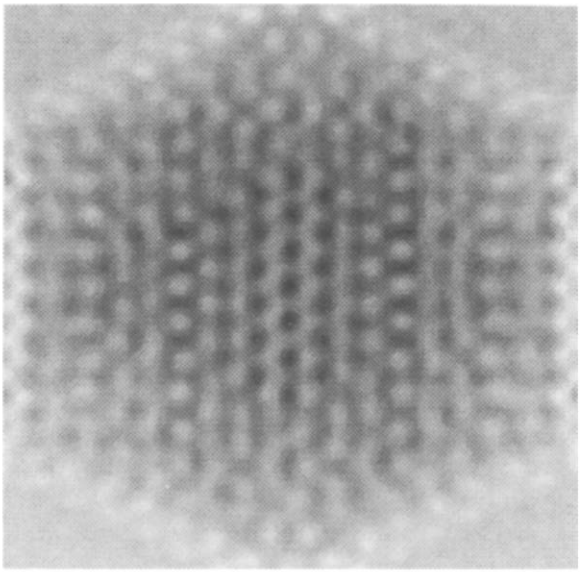

Pt Z=111 V=400 KeV Df=700 Å Cs=1.0 mm

Fig. 9. Calculated images of a cubo-octahedral particle with a ⟨111⟩ orientation at different defocus. Note that the image is not well defined for several defocus values.

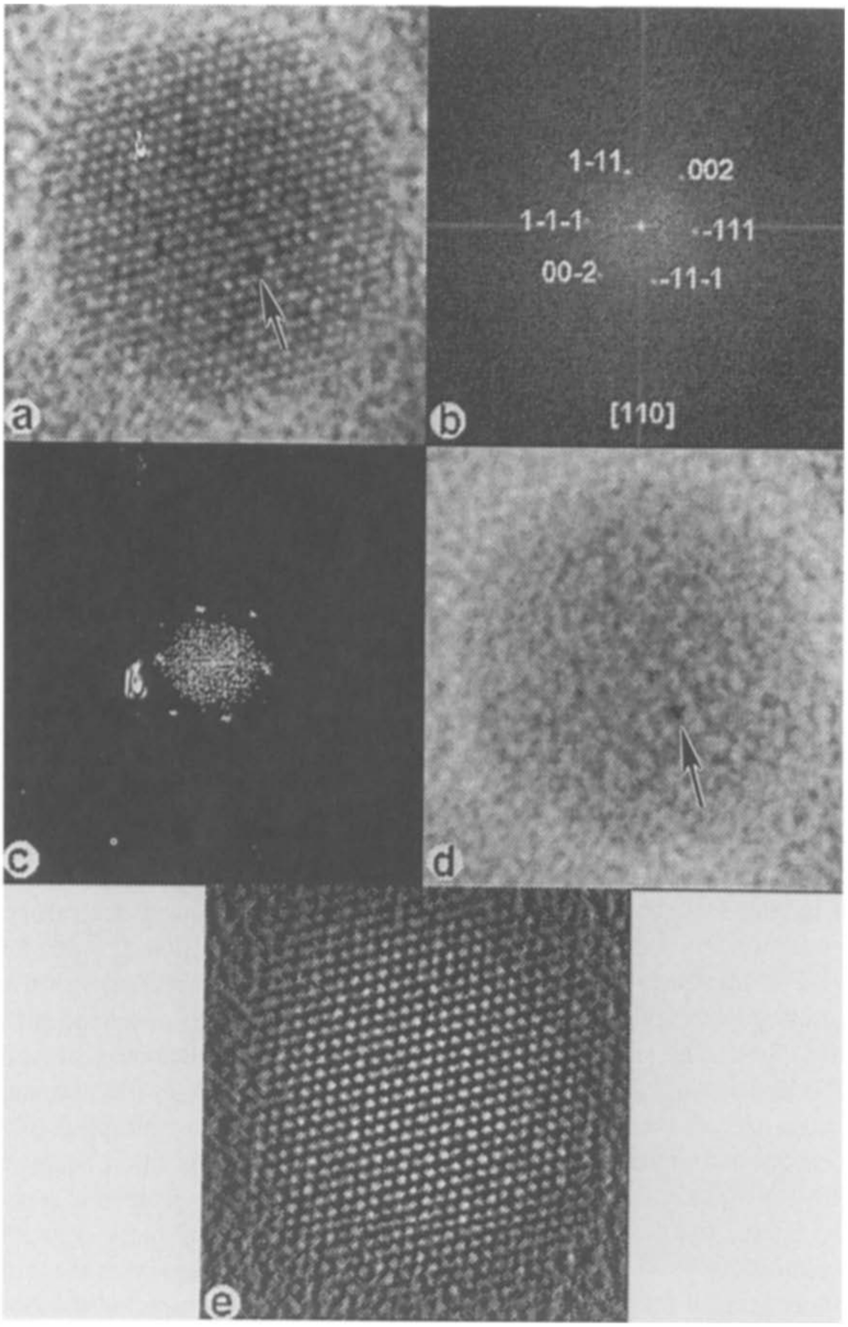

Fig. 10. Sequence that shows the image processing procedure. (a) Original high-resolution image of a Pt catalyst particle. (b) Fast Fourier transform (FFT) of the image in (a). The pattern can be indexed as a ⟨110⟩ orientation. (c) The mask applied to the FFT to black all the contributions from the particle. (d) The image produced using the mask in (c). It represents all the support contribution. (e) The image obtained by subtracting the image of the support (c) from the original image. The resulting image is more defined and some spurious features have disappeared.

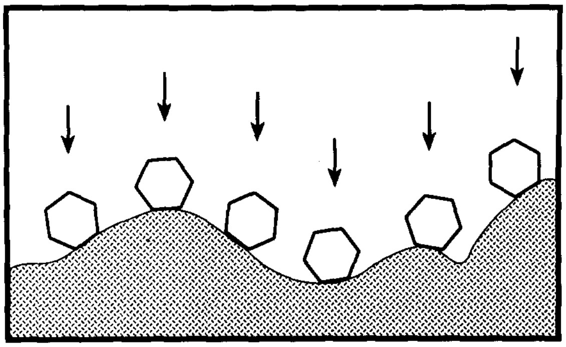

Fig. 11. The orientation of particles with respect to the electron beam in a typical supported catalyst might be random.

step we Fourier transform again the filtered signal and obtain an image which is cleaner than the original image. It should be always considered that image processing can improve the signal to noise ratio in an image. Extreme caution should be taken in the image processing to avoid the introduction of artefacts on the image. The technique is shown schematically in Fig. 3.

It should be stressed that the Fourier transform of a micrograph is similar in many ways to a direct diffraction pattern. In normal microscopy the diffraction pattern is basically the Fourier transform of the atomic potential in the sample, whereas the transform of the micrograph is essentially the transform of the modulus of the wave function leaving the sample and the microscope as described above. The transform of the micrographs carry crystallographic information similar to that of the diffraction patterns themselves. In other words the distances and angles between spots in a FT can be used in the same way as a regular diffraction pattern to find out the orientation of a nanoparticle. Spot splitting, arcing or broadening can be interpreted in a similar way to the standard diffraction.

A somewhat more general form of processing involves instead of a mask, a convolution with some filtering function S, in this case the filtered image I′ is related to the unfiltered image I by means of

$$I' = I * S$$

A good and important example of this is provided by the 'Mexican hat' function

$$S = (1 - \lambda^2 x^2 - \lambda^2 y^2)(\exp(-\lambda^2 x^2 - \lambda^2 y^2))$$

where λ is a (scaling) parameter. Actually this is a form of the so-called wavelet transform.

In the realm of small particles these transforms are useful basically because of their edge revealing capabilities. In Fig. 4a simulated particle is shown together with its transform; in this case it is apparent how the external shape of the particle is emphasised [18].

An altogether different form of processing is provided by a whole range of tools not based on the Fourier transform. A good example of this is provided by the algorithms devised for the purpose of revealing with accuracy the actual positions of columns of atoms in small particles. The algorithm works basically as follows: first a neighbourhood is defined such that it includes the whole area of the intensity peak representing the position of an atomic column and excludes any other peak. It is necessary first to generate an image that includes all such neighbourhood masks. By working selectively on each of the neighbourhood masks, an algorithm can evaluate the position of each peak and elaborate a list of coordinates.

A mask defining the border of a particle can be obtained by applying several methods; in some cases low-pass filtering can define the border appropriately, Fourier transform methods can also be used [19], as described above. In order to ensure that the whole nanostructure is included in the mask, sometimes it is necessary to expand the border with binary morphological erosion algorithms [20]. It is often necessary to obtain an enhanced image from the original micrograph more suitable for mask segmentation [21]. A selective enhancement of the atomic column can be achieved by targeting the Gaussian nature of these peaks and applying geometrical filters with Gaussian templates or correlation algorithms with Gaussian auxiliary functions.

The final neighbourhood mask is obtained by simple segmentation with a threshold [22] or with

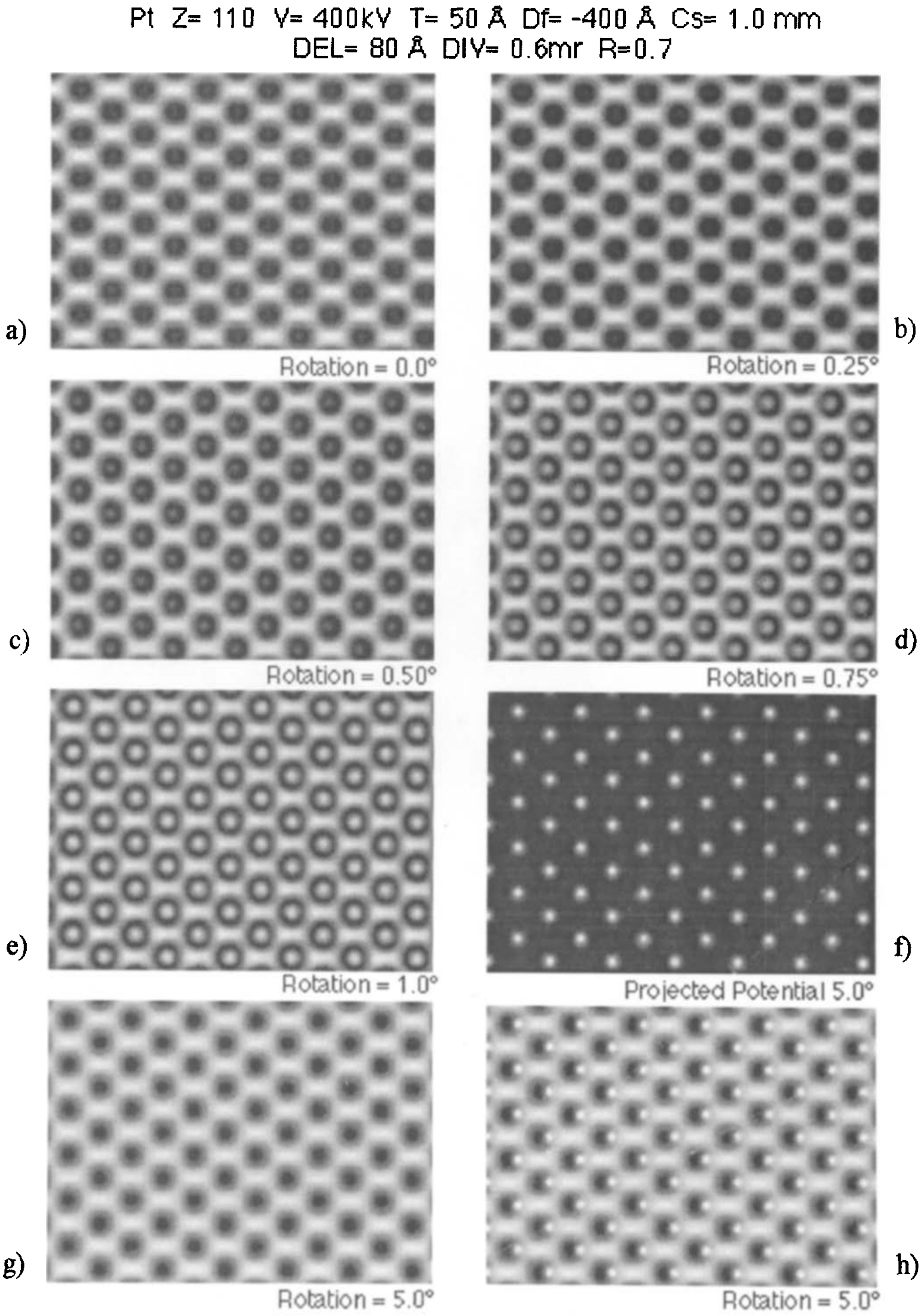

Fig. 12. Calculated image of a flat crystal of Pt oriented with the $\langle 110\rangle$ direction parallel to the electron beam. The real atomic positions are shown on the image. (a) Condition at which the beam is parallel to the $\langle 110\rangle$ axis of the crystal. Images after tilting off the axis, (b) 0.25°, (c) 5.0°, (d) 0.75°, (e) 1.0° and (f). Projected potential 5.0 (g). (h) Superimposed image of the 'real' atomic positions on the image obtained after 5.0° tilting.

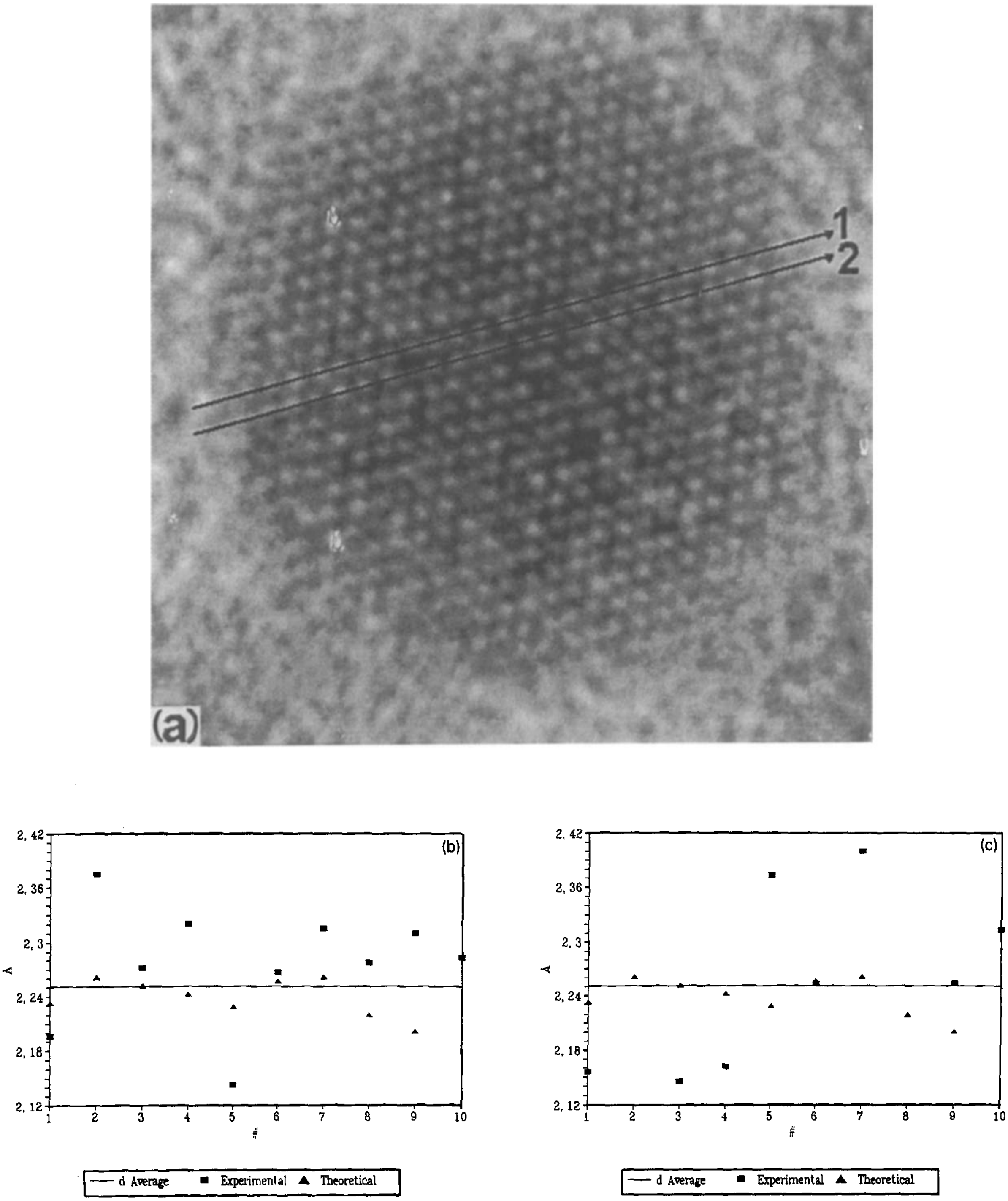

Fig. 13. Plot of the distance between spots along a line crossing a Pt particle oriented in the ⟨110⟩ direction vs. the position of the atomic column. The expected average value is shown in the figure by a solid line. The corresponding experimental points are indicated by □. The plots also shows the theoretical values indicated by obtained for an undistorted particle with the same ⟨110⟩ orientation. The variations are due to the dynamical nature of the diffraction through a particle. (a) Image of the particle showing the lines used for the experimental data. (b) Plot for line 1. (c) Plot for line 2.

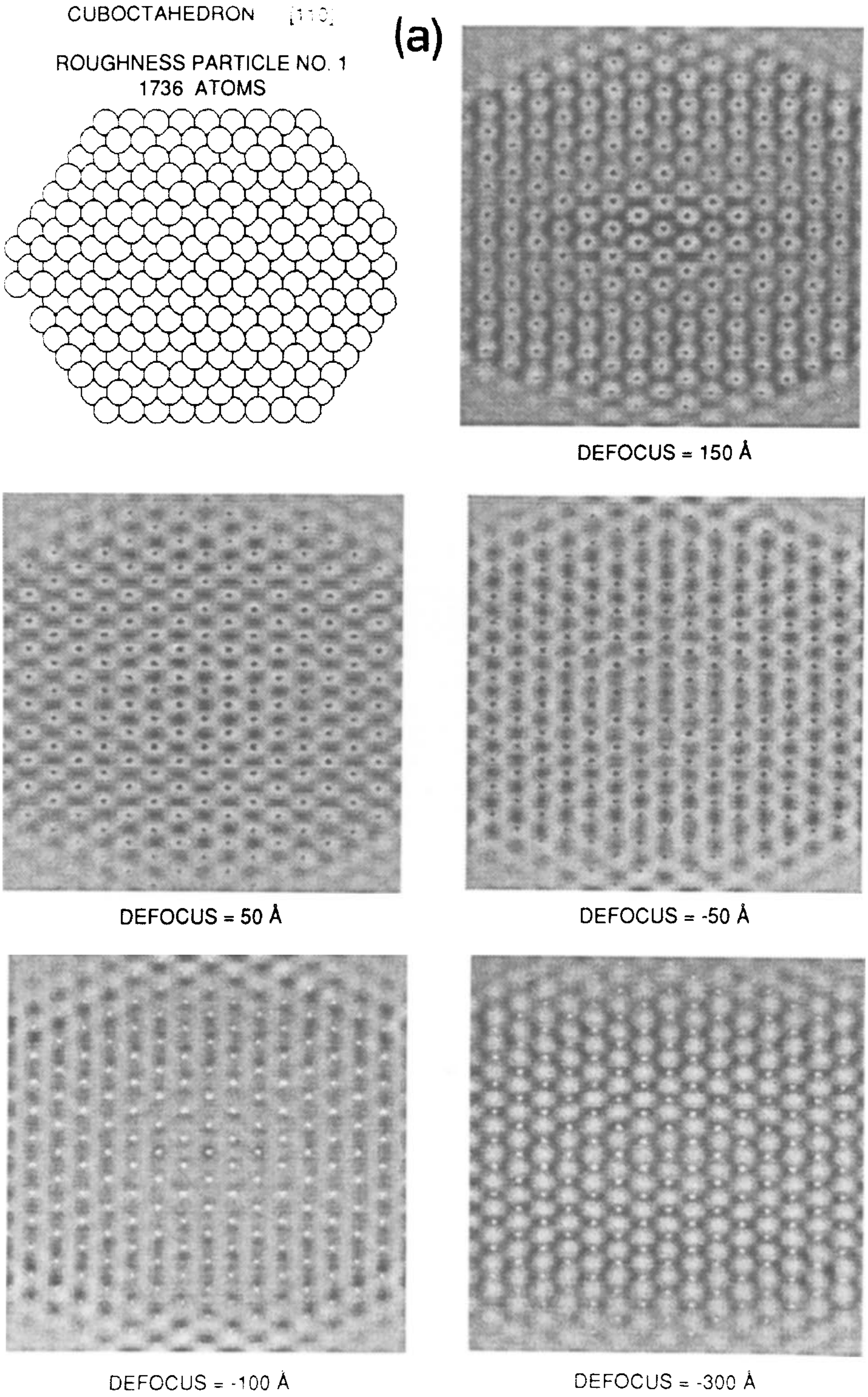

DEFOCUS = 150 Å

DEFOCUS = 50 Å

DEFOCUS = -50 Å

DEFOCUS = -100 Å

DEFOCUS = -300 Å

Fig. 14. Calculations of particles with different degrees of roughness and their corresponding calculated images at different defocusses. (a) Particle of 1736 atoms with a small degree of roughness. (b) Particle of 1360 atoms with a larger degree of roughness. (c) Particle of 1468 atoms with a larger degree of roughness than (a) and (b). (d) Particle of 1474 atoms with a very extended roughness. It is clear from the image that the roughness produces a random shift in the inter dot distance similar to the one observed in the experimental images (Fig. 13).

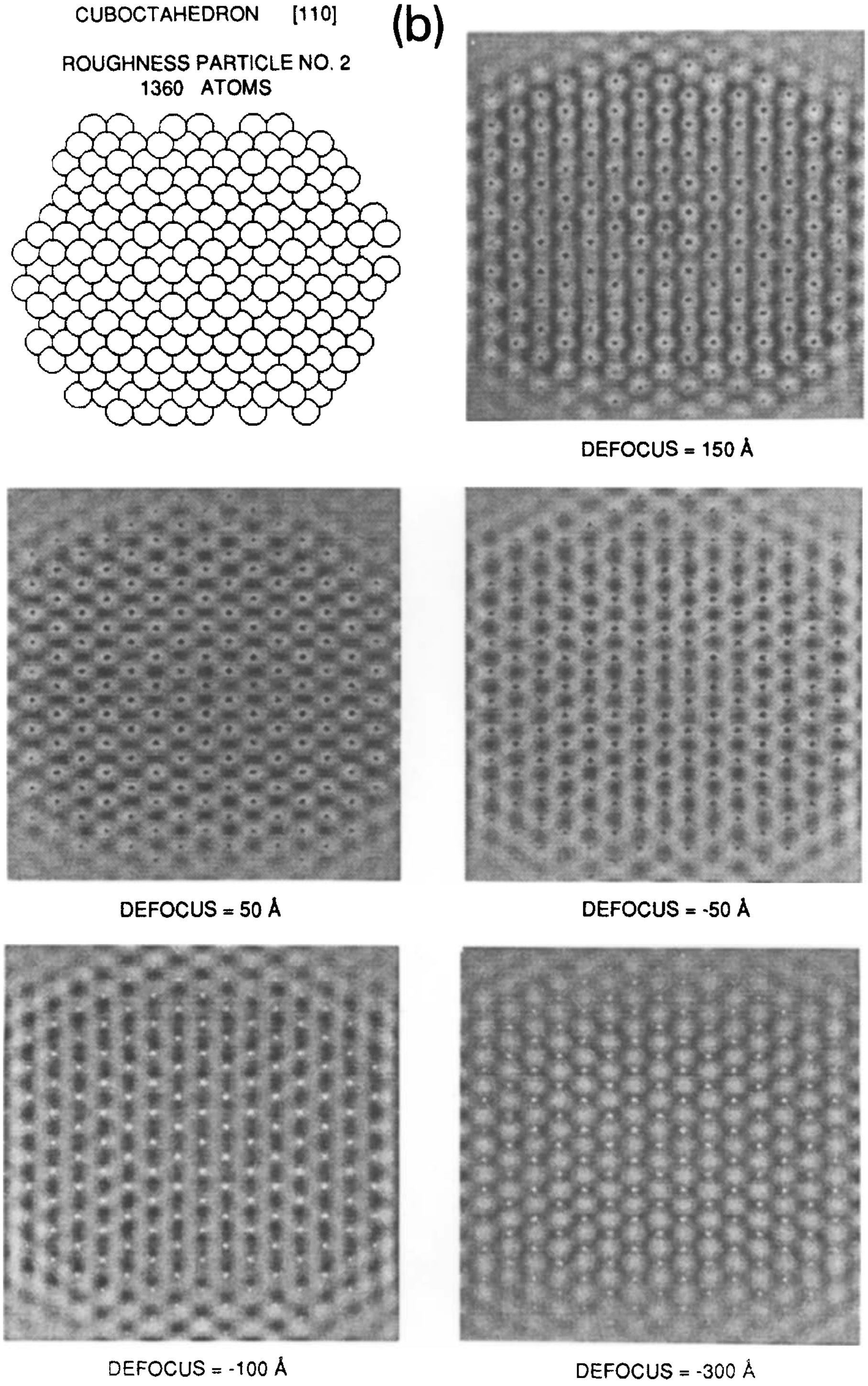

DEFOCUS = 150 Å

DEFOCUS = 50 Å

DEFOCUS = -50 Å

DEFOCUS = -100 Å

DEFOCUS = -300 Å

Fig. 14 (continued).

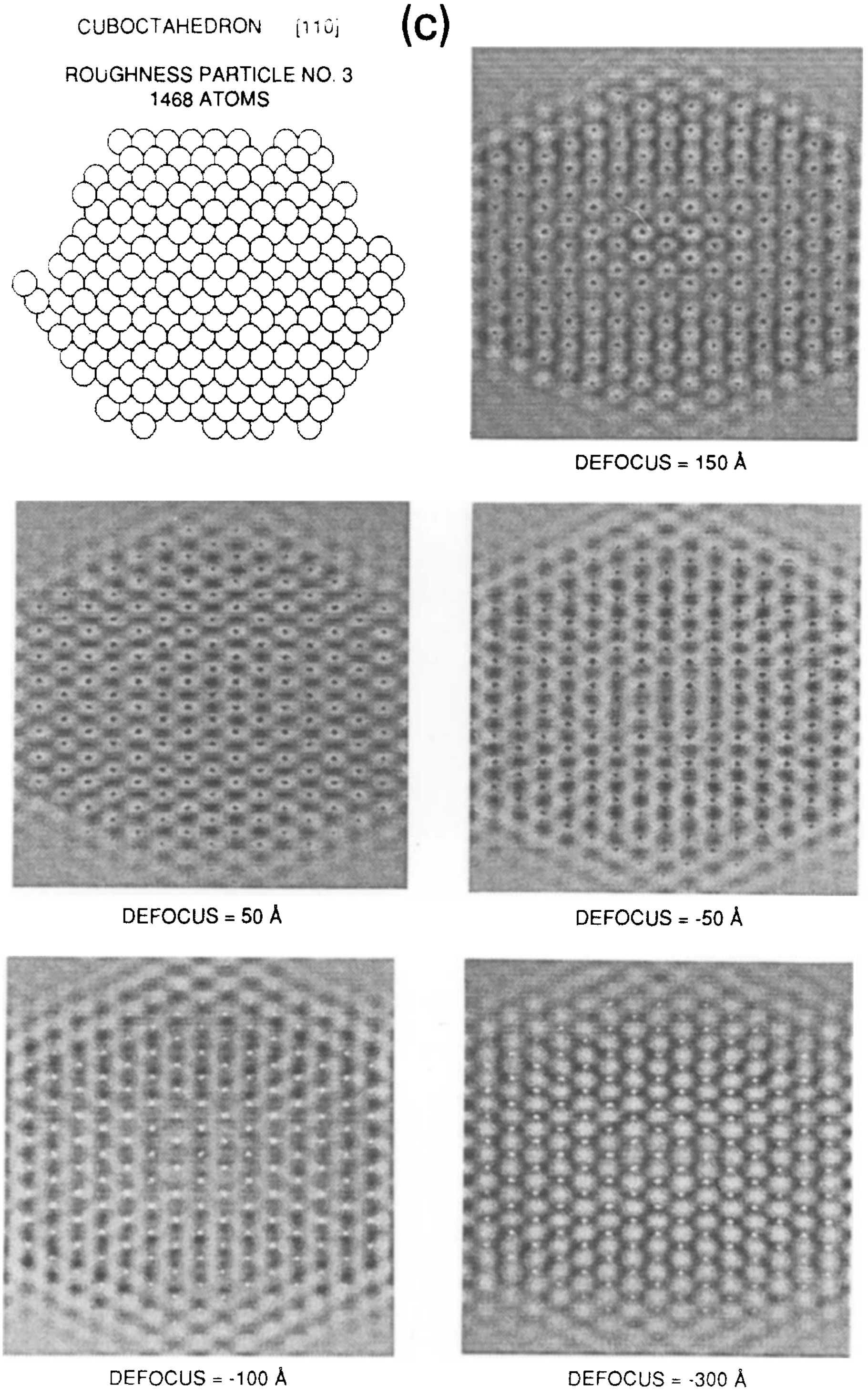
CUBOCTAHEDRON [110]
(c)
ROUGHNESS PARTICLE NO. 3
1468 ATOMS
DEFOCUS = 150 Å
DEFOCUS = 50 Å
DEFOCUS = -50 Å
DEFOCUS = -100 Å
DEFOCUS = -300 Å

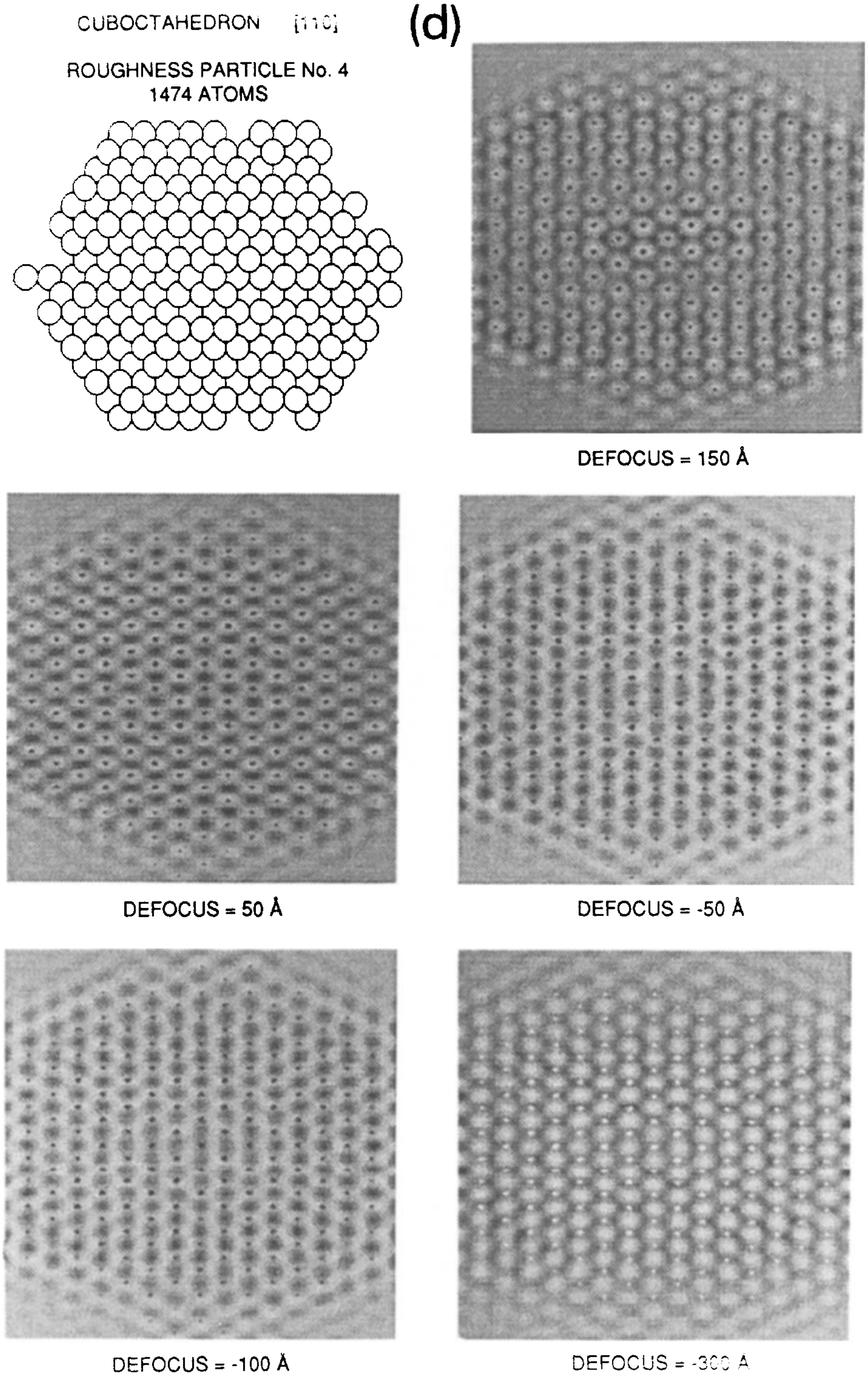

Fig. 14 (continued).

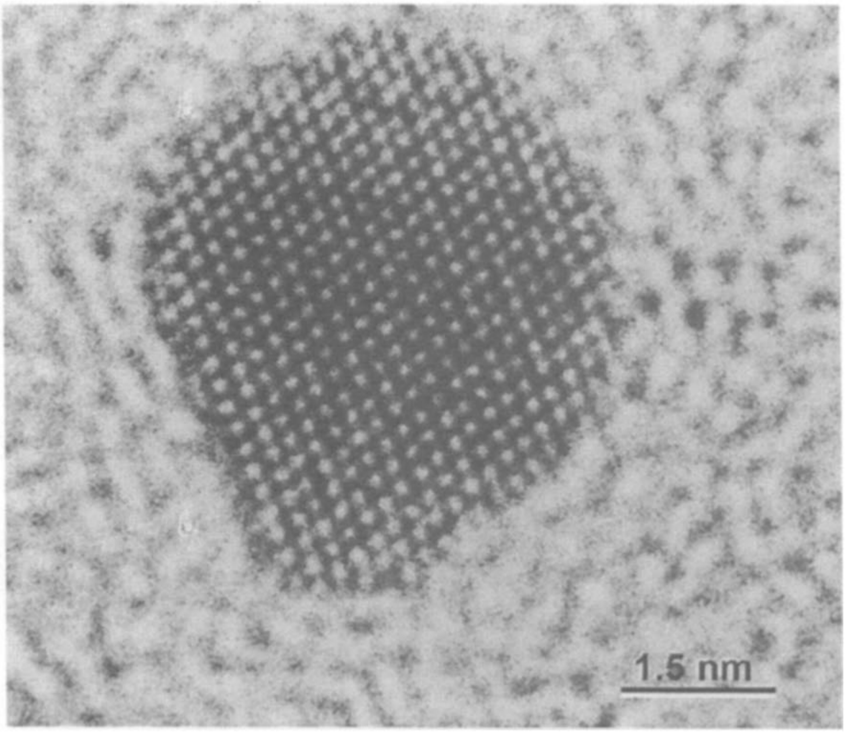

Fig. 15. Experimental image of a Pt catalyst particle with atomic resolution. The fading contrast at the edges is due to roughness as shown in Fig. 14

an Otsu algorithm [23]. For each neighbourhood the contribution of the position of the pixels can be averaged with different weighting criteria in order to obtain a representative set of coordinates. Once the list is obtained, with the help of geometric selection algorithms, columns can be classified as belonging to different domains, planes, particles etc. and the adequate sub-lists can be generated; these lists can be useful in processes like automatic crystalline structure characterisation.

In Fig. 5 the process is applied to a grain boundary in a metal catalyst; the figure shows a reconstruction of an experimental image. The reference (average) lattice has also been calculated for comparison purposes and the deviations from the ideal lattice are clearly visible. In this figure the (average) lattices are plotted with the scale indicated in the legend at the right; the actual (deviated) atoms are plotted in a grossly exaggerated manner (according to the scale for deviations in the legend).

4. Image calculations of small particles

In order to calculate images of the particles a first question that has to be answered is what is the most proper interatomic potential to use in the calculations. The answer might come from a recent paper by Mulder et al. [24] who have shown using Mössbauer spectroscopy that a Pt cluster as small as 150 atoms might already exhibit the metallic bonding behaviour. This important result, implies that using metal coefficients is not a bad approximation. Therefore we should expect that the electron scattering by the particles will present a strong dynamical character. Therefore kinematical theory or even two-beam dynamical theory will not be useful in this case. The use of N-beam dynamical theory will be necessary.

In the present work we have used a dynamical software developed by our own group [25]. This package has the advantage that no crystal periodicity is required for doing the calculations. The atom positions are directly fed. Therefore samples with a non-conventional crystallographic structure such as icosahedral or decahedral particles can be easily calculated. Other programs are available which also permit calculations of small particles [26].

A second important point to address is which is the most convenient condition for observing the metal particles. Each black or white dot in a HREM represents a column of atoms; under the proper conditions, the dot should represent the projection of the column along the beam direction. However, there is not necessarily one-to-one correspondence of the image position with the real position. The thickness might play a role in shifting the images. Fig. 6 shows an example of a cubo-octahedral particle along the ⟨100⟩ orientation. In the calculated image the atoms appear as white

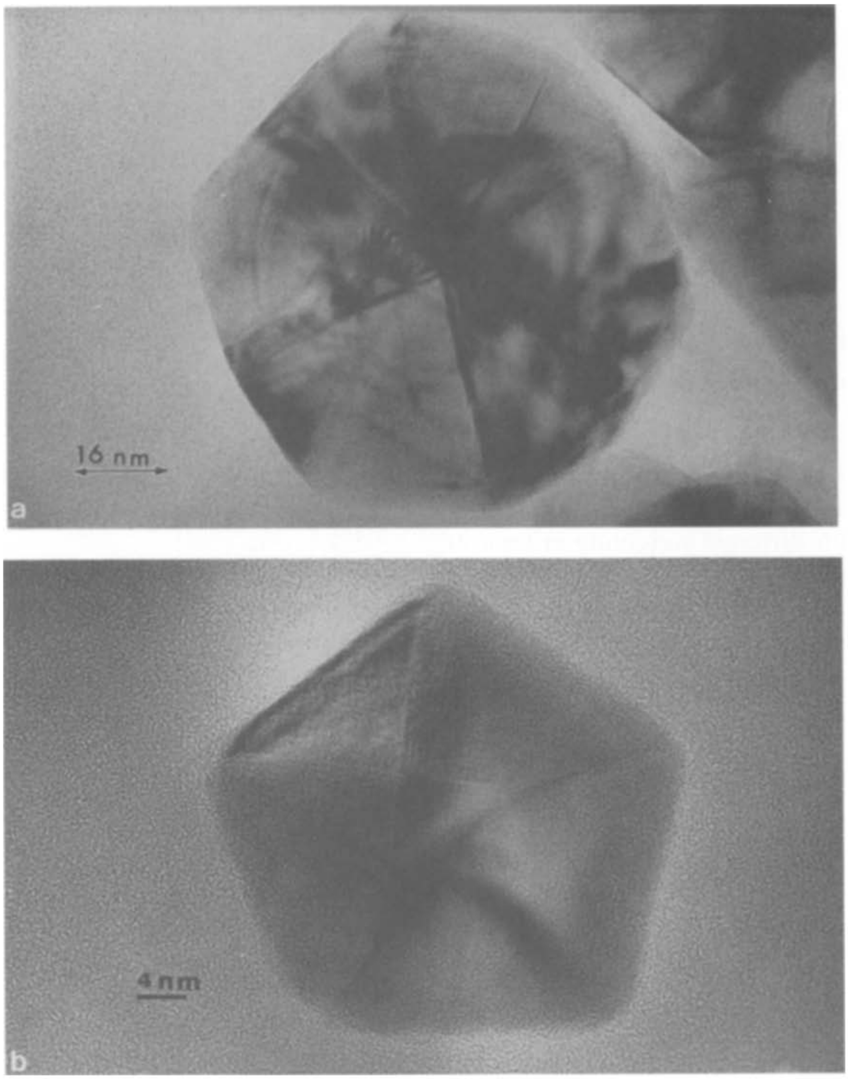

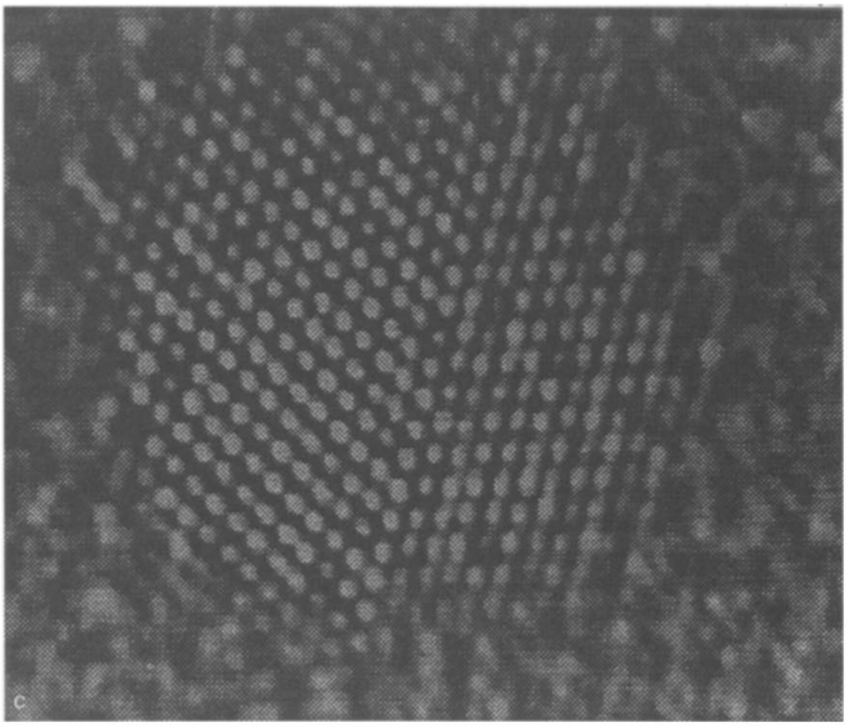

Fig. 16. Images of Pd–Au bimetallic particles obtained by colloidal methods. (a) Particle with an icosahedral shape. (b) Particle with a decahedral shape. (c) Particle with a single twin.

dots. We have superimposed on the image the real positions of the atom columns. As can be seen a shifting of the images is produced as the thickness of the atomic columns varies. In the figure we also show the number of layers that each atomic column contains. This effect appears to be more pronounced at thin portions of the sample. This effect has to be considered because otherwise, false lattice distortions might be inferred from the images.

Another point to consider is the optimal conditions for image contrast transfer. The principles have been already discussed in Section 2. A useful way to visualise the conditions is to plot the image contrast vs. defocus for a given spatial frequency on the image (the reciprocal of lattice interplanar distance). Fig. 7 shows the curve for the case of a gold particle showing the frequencies corresponding to the (200), (220) and (111) planes, which are the most commonly observed. As can be seen optimal conditions are produced at a defocus of ca. 55 Å. At this condition we can see also simultaneously the particle (111) and (200) planes. Similar conditions can be found in other noble metals which are commonly used in catalysts.

Calculations of images of particles require a large amount of CPU time. The first calculations using a realistic size particle were made by Fluei [27] using a Cray computer. Nowadays similar calculations can be performed using parallel array processors. In Fig. 8 and Fig. 9 we show a calculation for a cubo-octahedral particle. Fig. 8 shows the image produced at different defocus conditions for a ⟨110⟩ oriented particle (the cluster in the upper figure seems to be larger than the cluster in the lower one, this is an artefact of defocus, both images refer to the same cluster). Fig. 9 shows the corresponding set of images for a ⟨111⟩ particle. In both cases the direction is along the electron beam and it is assumed perpendicular to the substrate. We can see that the image of the ⟨110⟩ oriented particle is very clear in several defocus conditions. The image of the ⟨111⟩ particle on the other hand is not well defined for a large number of focusing conditions. If caution is not taken it will be very easy to confuse $\langle 111 \rangle$ particles because the expected hexagonal array of atoms will not be observed. It is technically now possible to have the microscope on-line with a fast enough computer that will allow the observation of HREM images and compare on-line with the corresponding computed image.

5. Effect of the support

In the study of nanoparticles in real catalysts the support plays a very important role. The most common substrates, γ-Al_2O_3, SiO_2 and graphite are crystalline at the nanoscale and therefore scatter the electrons coming out of the metal particle. Even if the substrate is amorphous it reduces the intensity of signal from the particles. The theory for this case has been worked out by José-Yacamán and Avalos Borja [28]. A crucial point is the orientation relationship between the particle and the substrate. It is always desirable to orient the electron beam in such a way that the particle is strongly diffracting and the substrate is not. This produces the optimum conditions for particle imagining. However, this kind of orientation is very difficult to achieve and in many cases impossible because of the orientation relationship between particles and the support. However, in the case of high-resolution images of catalysts the image processing can be invaluable. Fig. 10 shows the example of a Pt particle supported in amorphous carbon. Fig. 10a shows the original image of the particle obtained at the optimum focus con-

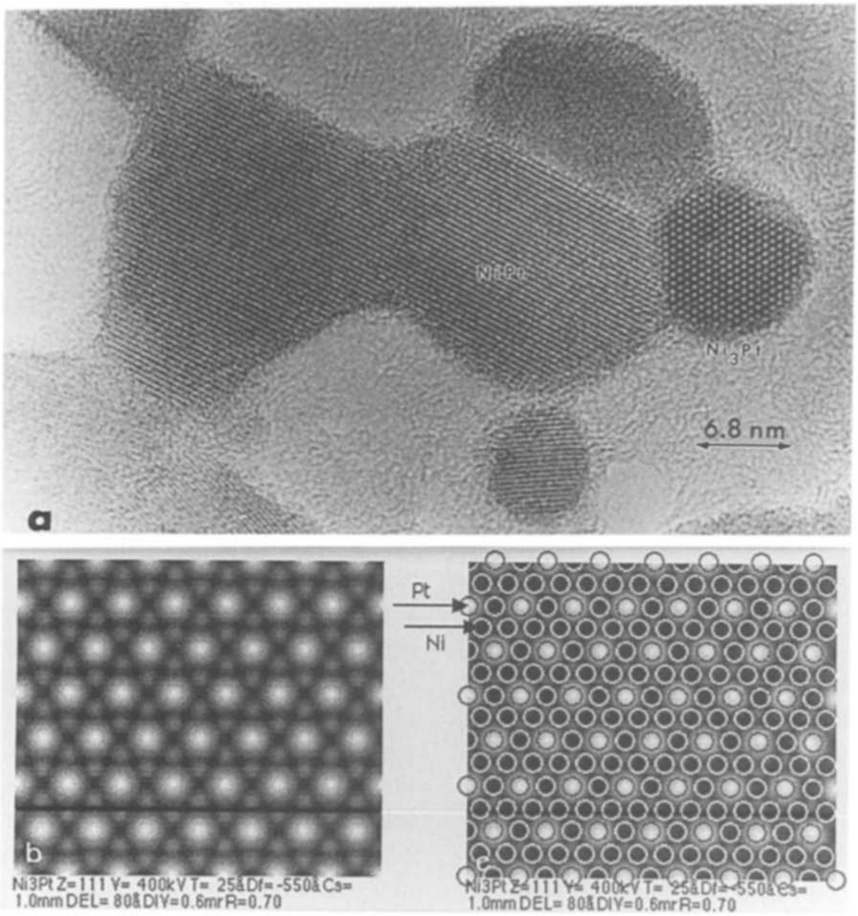

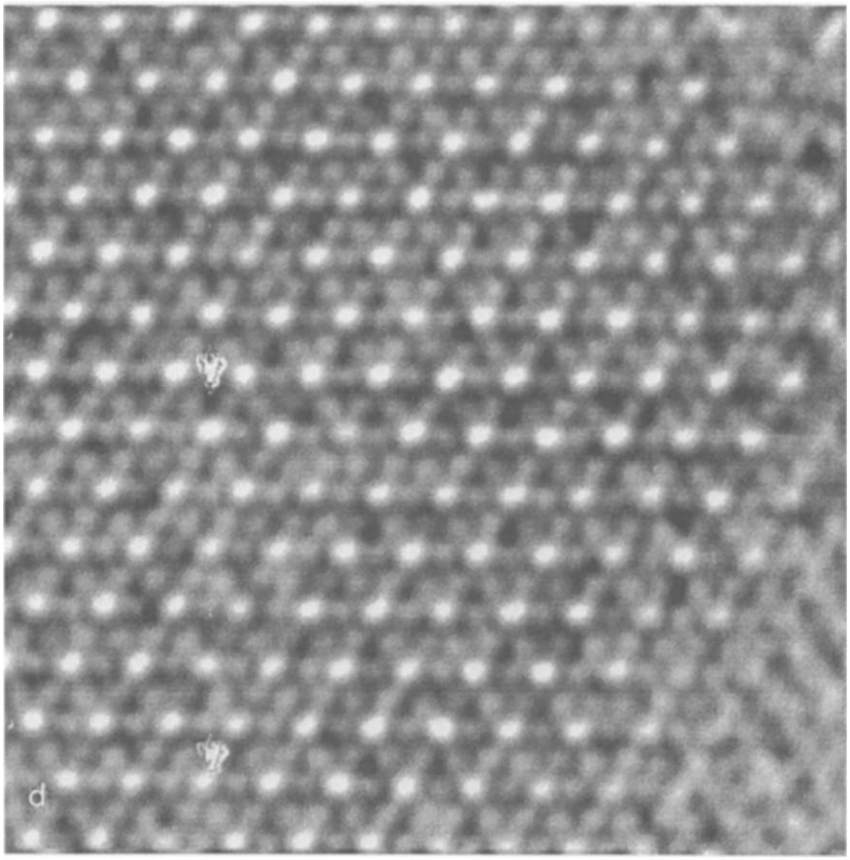

Fig. 17. (a) High-resolution image of a Pt–Ni particle. (b) Image simulation of the Ni_3Pt phase. (c) Same calculated image showing the position of Pt atoms (black dots) and Ni atoms (white dots). (d) Amplified image with enhanced contrast of a portion of the image in (a).

dition. The Fourier transform (Fig. 10b) of the particle shows the spots corresponding to the particle which appear well defined plus the background spots due to the support.

We now apply a mask to the spots of the particle as shown in Fig. 10c. The spots should be identified by indexing the spots the same way that we index the spots of a diffraction pattern. In the case of the particle in Fig. 10, the orientation corresponds to $\langle 110 \rangle$. By Fourier transforming again, we now obtain an image corresponding to the support as shown in Fig. 10d. This image although basically structureless contains some interesting contrast variations. If we now produce an image by subtracting Fig. 10a from the image of Fig. 10d we obtain a new image that corresponds to the particle without support. As can be seen in Fig. 10e, the particle looks much cleaner. In fact many of the irregular features that are apparent in Fig. 10a have now disappeared. For instance, in the region marked with an arrow in Fig. 10a it appears that the particle contains a distorted region. The same region in Fig. 10d is shown by the arrow and a black feature can be seen. In Fig. 10e the feature has disappeared. Therefore, we can conclude that this irregularity was not real and resulted on the image only as an artefact of the substrate. This shows that erroneous information can be obtained in HREM pictures of supported catalysts if caution is not taken. In addition image processing can do the trick for us of eliminating the blurring of information on the catalysts due to unwanted contrast of the substrate. Recently an extensive study of the effect of the support on HREM images has been published by Yao and Smith [29].

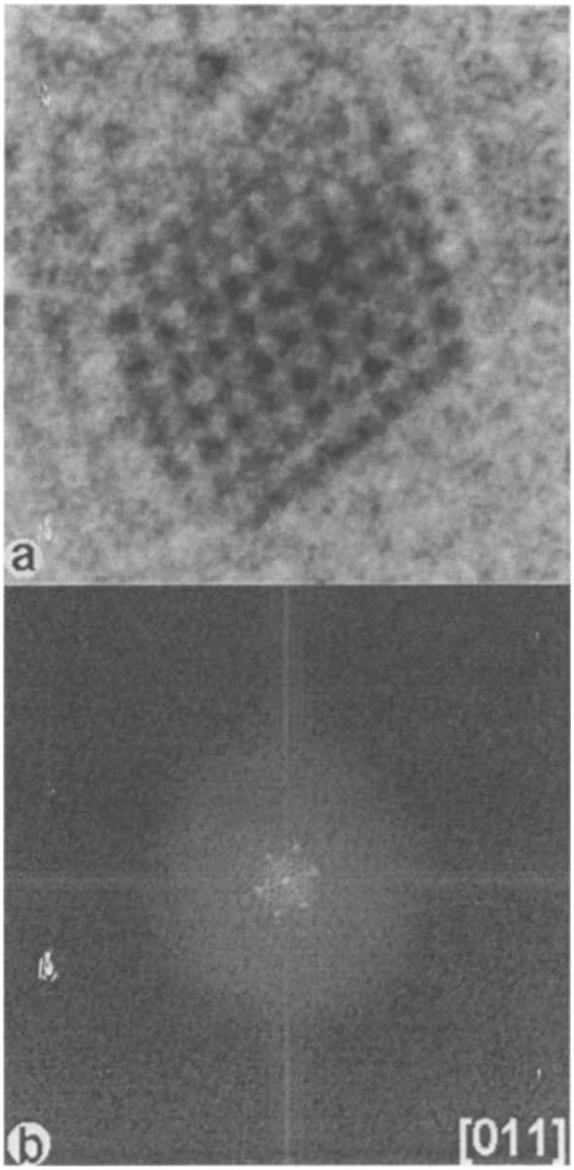

Fig. 18. (a) Image of a Pt particle on a $\gamma\text{-Al}_2\text{0}_3$ support. (b) Fourier transform showing the ⟨011⟩ orientation.

6. Effect of orientation and particle statistics

One main problem of observing small particles using HREM is that often the particles are randomly oriented with respect to the electron beam as shown in Fig. 11. It is known that the contrast and altogether the possibility to achieve atomic images will depend on the orientation. After all high-resolution images in the best conditions represent a projection of the structure along the electron beam direction. If we have a low index direction we expect that dark dots will correspond to atomic columns of the structure. The question that arises is: how far from the exact low index orientation the electron beam can be before the best conditions are lost?.

We have made a systematic study for the case of Pt particles. Fig. 12 shows the image of a flat crystal of Pt oriented with the ⟨110⟩ direction parallel to the electron beam. The image was calculated for a defocus of $\Delta ff = -405$ Å. Fig. 12a represents the condition in which the perfect orientation is achieved. Fig. 12b–h represent the image that is produced after tiltings of 0.25°, 0.50°, 0.75°, 1.0° and 5°. The tilt axis was along a ⟨110⟩ axis. The changes at first sight do not look so dramatic.

However, Fig. 12h shows a superposition of the 'real' atomic positions (projected potential) superimposed on the image obtained after 5° tilting. As it is possible to see from the figure the dots in the image are shifted with respect to the real atomic positions, which makes the image useless for full analysis. The same effects are observed probably for the tiltings of Fig. 12. The conclusion of our calculations will indicate that a 0.5° change in orientation is enough to produced changes on the image which are significant. If an image of a large area containing several particles is obtained no general information about the system can be obtained because of the effect shown in Fig. 12. A sad conclusion can be reached: small particles can only be studied one at a time. If the sample contains 500 particles in a field of view of say one millimetre, it will mean that we have to obtain tilting and defocus images from at least one thousand particles. This task is clearly impossible. Therefore we might end up extracting general information such as crystal structure, atomic composition from an area that is not representative of the sample. This problem requires serious consideration but several 'rules of thumb' should be applied in order to get useful information from catalytic samples using TEM.

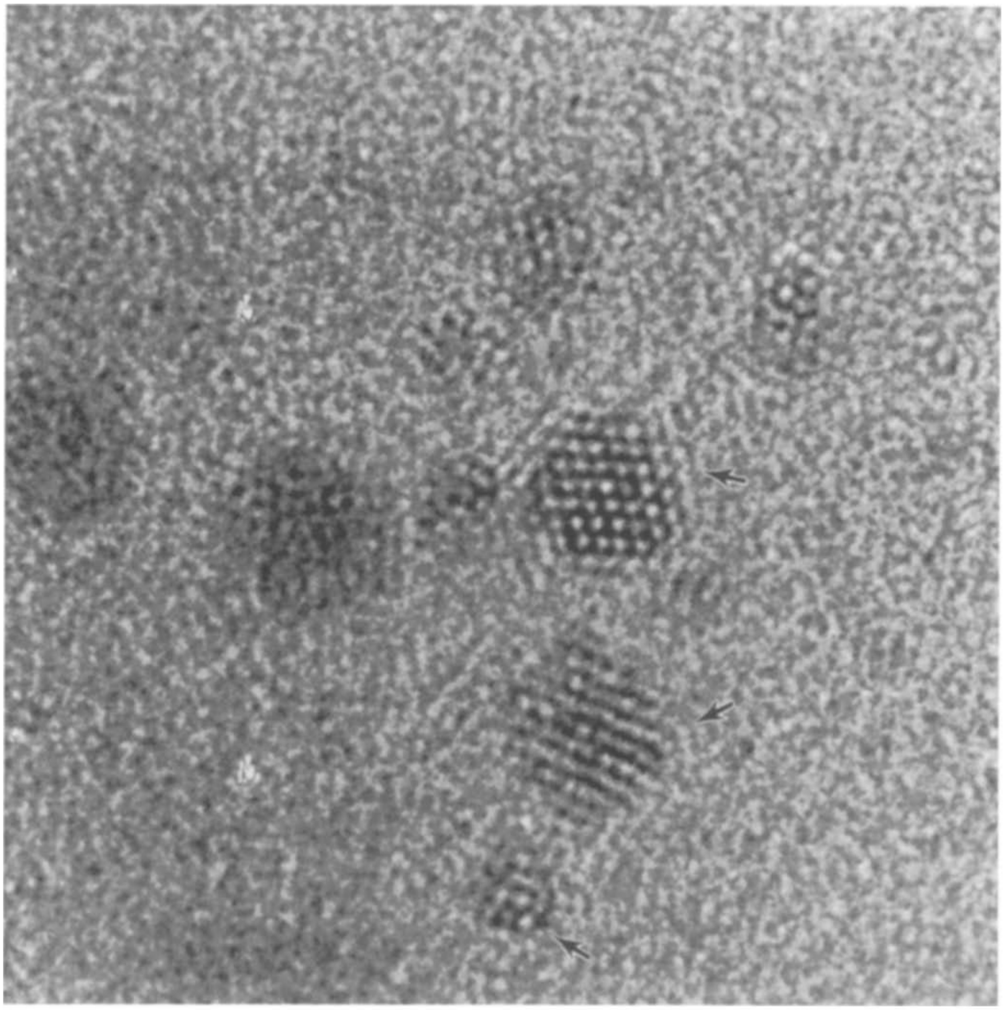

Fig. 19. HREM image of Pt particles grown by vacuum evaporation showing an asymmetric shape indicated by arrows.

It is necessary to perform a minimum of statistics. Several regions of the sample should be recorded. On-line computer processing will allow the examination of a considerable number of particles in a short time.

The microscopy has to be as complete as possible. We have to match HREM with X-ray microanalysis and EELS. This will necessitate that we compare regions with similar chemical composition.

Medium resolution examination of the samples will be necessary to obtain general information about the sample and then apply HREM to characterise the portion of the sample of most interest.

- TEM is a local characterisation technique and has to be combined with techniques that can give information averaged over large areas such as: X-ray diffraction, NMR, infrared spectroscopy and so on.

In catalysis the problem is which multitechnique approach is required to be solved. The combination of local and average information can give important clues in solving a specific problem.

7. Effect of thickness and particle roughness

We have a particle with 3-D such as an cubo-octahedron. The atomic columns seen by the elec-

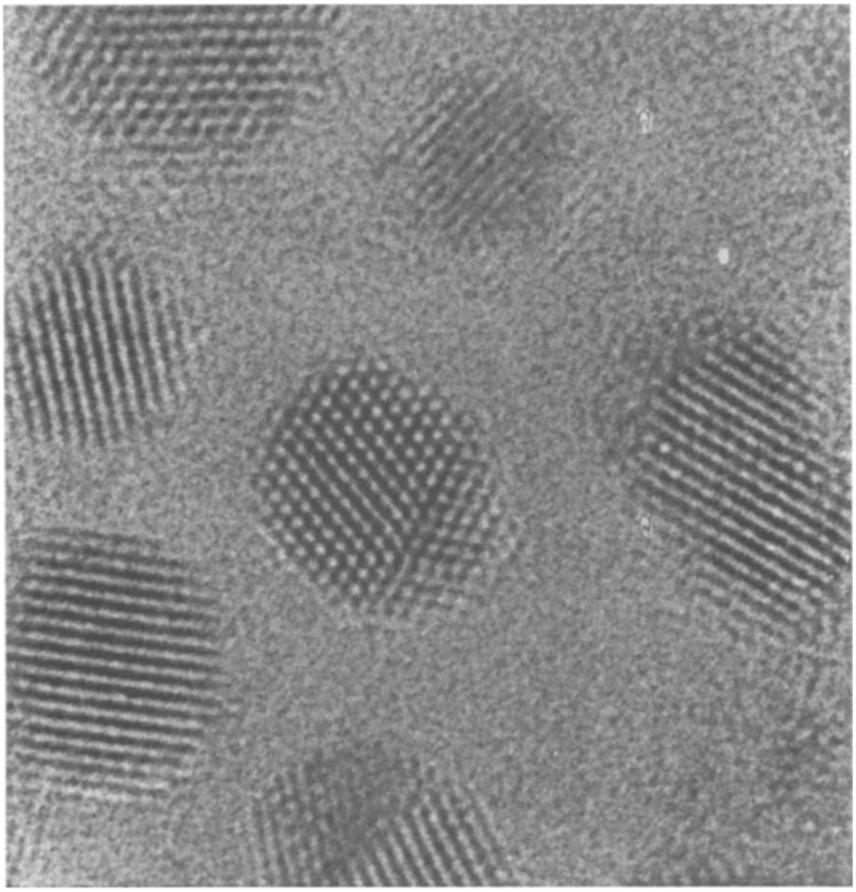

Fig. 20. HREM of evaporated Pt particles that have coalesced into a larger one. Note that the structure is single crystalline in large portions.

tron beam have a different number of atoms i.e.; the thickness of each column is different. Fig. 6a indicates this effect for the case of cubo-octahedral particle oriented along the ⟨100⟩ axis. This thickness variation has a strong effect on the image. As shown in the calculated image in which the real atomic positions (black dots) are superimposed on the image (white dots). As it is clear from the figure the image spots shift with respect to the real position. This effect was first discussed theoretically by Fluei [27] and confirmed on experimental images by M. José-Yacamán et al. [30].

This effect can be used to analyse the roughness on nanoparticles. We refer again to the particle in Fig. 10. In this case we have measured the distance between spots along a line crossing the particle along the ⟨111⟩ direction. In Fig. 13 we show the plot of the distance between spots along the line. It is clear from the figure that there are very large variations in the distance between spots up to 10%. When analysing a large number of pictures we found similar results. In order to obtain Fig. 13 a very careful calibration of the magnification of the microscope was necessary. On the other hand magnification errors alone will not explain variations in the same picture. The observed variations are well above the experimental error. A second effect that we considered was the possibility that the variations were due to image processing. In order to assess this effect we used a calculated image of a particle with cubo-octahedral shape oriented in the ⟨110⟩ direction. It was processed using the same algorithm that was applied to the real image and the distances were measured. We found that the distances between dots were not altered by image processing.

In order to reduce the errors in the localisation of the peaks of Fig. 13a we used the algorithm developed by Beltrán del Río et. al. [31] which takes advantage of the gaussian nature of the peak and locates a peak with a high degree of accuracy. We also consider the possibility that the variations observed in Fig. 13 were the result of the dynamical effects produced during image formation. Indeed it is conceivable that the complex interaction between the electrons and the atoms of the particle might result in random variations on the distance. In Fig. 13b the distances between atomic columns in an ideal undistorted $\langle 110 \rangle$ oriented particle indeed show variations. The variations are due to the dynamical nature of the diffraction through a particle. The inset shows the line of atoms used to obtain the data. However, these oscillations are below the level observed experimentally as shown in Fig. 13b. We can also exclude the effect of misorientation of the particle as we discussed in the previous section.

We are left only with three possibilities; the observed variations are due to a true distortion of the lattice, they are due to surface roughness, or they are due to the substrate. The first possibility is unlikely, remembering that each bright spot represents an atomic column, therefore the whole column will have to be expanded or contracted. The theoretical work on this problem indicates that this is not the way in which the particle should be distorted.

The fact that the substrate has an effect on the images of atomic columns and, in particular, that it affects the apparent positions, can be estimated. Consider the substrate as consisting basically of a series of terraces and wedges.

The effect of a single wedge on the image of an atom can be assessed as follows: (1) if the mean potential of the wedge is V, and the atom is assumed to be at a distance Z from the substrate, then the wave function at the substrate is given by

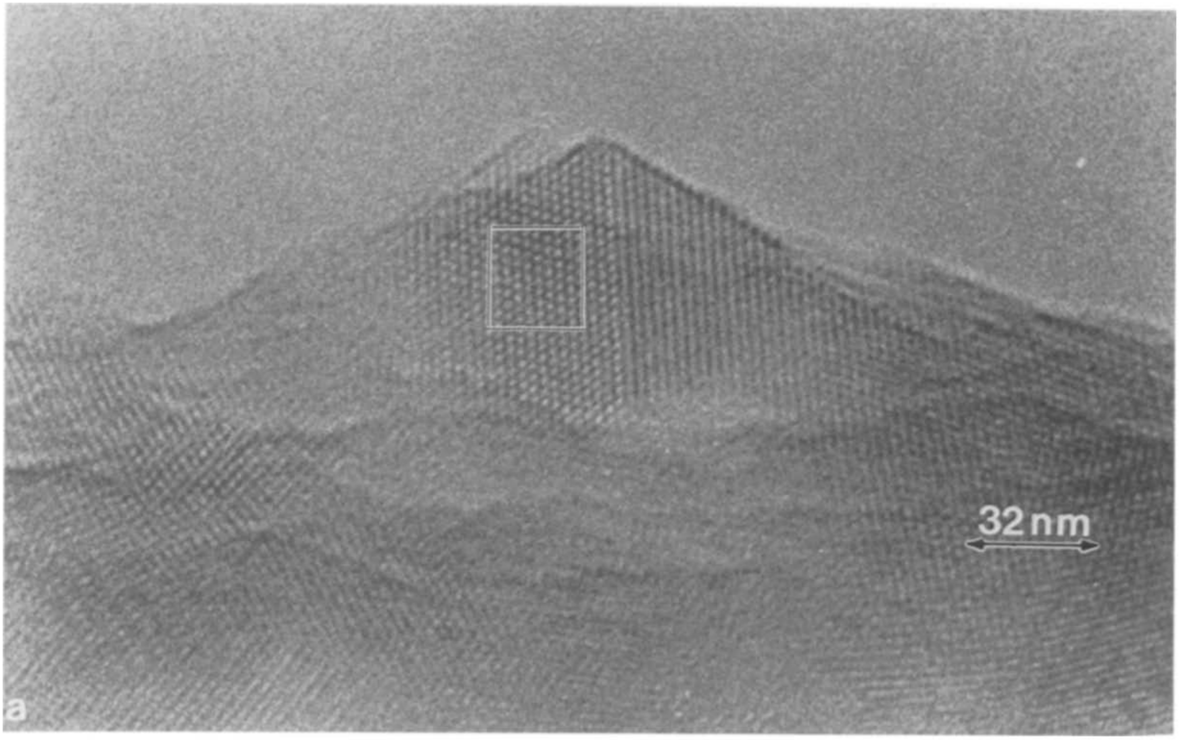

Fig. 21. Image of microcrystalline Al_2O_3 after heating in H_2S/H_2 atmosphere. (a) HREM image showing crystallisation. (b) Another region.

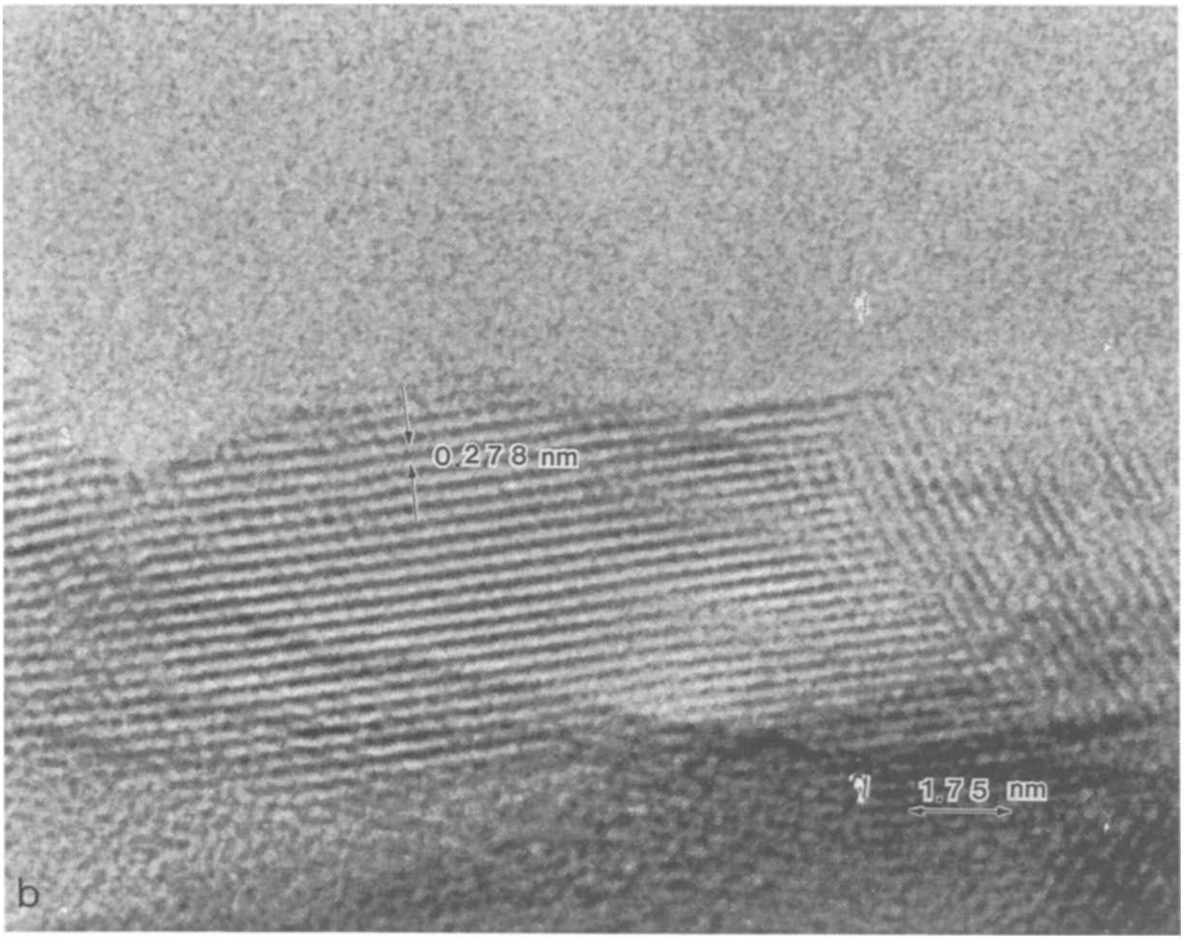

Fig. 21 (continued).

$$\frac{-i}{\lambda z}\,\mathrm{e}^{2\pi i\chi z}\,\mathrm{e}^{i\pi[(x^2+y^2)/z\chi]}\,\mathrm{e}^{im\sigma V_p}$$

where σ is the interaction constant and V_p is the projected potential. The projected potential V_p in turn is given by

$$V_\mathrm{p}=mVx$$

where m is the slope of the wedge (for simplicity we took a wedge starting at depth zero and running in the x direction only). Here only the mean potential V is taken into account (that is, we are considering refraction effects by the substrate).

Consequently the observed image is given by the wave function

$$\frac{-i}{\lambda z}\,\mathrm{e}^{2\pi i\chi z}\,\mathrm{e}^{i\pi[(x^2+y^2)/\chi z]}\mathrm{e}^{i\sigma mVx}$$

that can be written as

$$\frac{-i}{\lambda z}\,\mathrm{e}^{2\pi i\chi z}\,\mathrm{e}^{i\pi\{(x^2+y^2)/z\chi\}+\sigma mVx]}$$

$$=\frac{-i}{\lambda z}\,\mathrm{e}^{2\pi i\chi z}\,\mathrm{e}^{(i\pi/z\chi)\,[(x^2+y^2)+\sigma mVxz\chi)]}$$

$$=\frac{-i}{\lambda z}\,\mathrm{e}^{2\pi\chi z}\,\mathrm{e}^{(i\pi/z\chi)[(x^2+y^2)+\alpha x]}$$

$$=\frac{-i}{\lambda z}\,\mathrm{e}^{2\pi i\chi z}\,\mathrm{e}^{(i\pi/z\chi)[(x^2+y^2)+\alpha x+\alpha^2/4-\alpha^2/4]}$$

$$= \frac{-i}{\lambda z} \mathrm{e}^{2\pi i \chi z} \, \mathrm{e}^{(i\pi/z\chi)[(x+\alpha/2)^2+y^2)-\alpha^2/4)]}$$

where

$$\alpha = \sigma m V z \chi$$

meaning that the image has been displaced by

$$\delta = \alpha/2 = \sigma m V z \chi/2$$

From this formula we can estimate that the shift on the images is smaller than the ones observed in Fig. 13. A study of the effect of the support (in the case of an amorphous) was performed by Paciornik et al. [32] and Saxton and Smith [33].

In order to further isolate the effect of the support on the shift of the images, we performed some measurements on particles that were located on a region near a hole on the support film. In this case the effect of the support is eliminated. In these samples we also observe shifts of the same order of magnitude as the ones observed in Fig. 13.

Therefore, surface roughness is the most likely effect. In Fig. 14 we show models of rough particles and the resulting images at different defocus conditions. As can be seen, the shift between image dots and real positions is of the order of magnitude of the observed ones. A further confirmation of the roughness effect can be obtained from the images of the particle edges.

The calculations of Fig. 14 show that because the roughness is more pronounced at the edges of the particle, atomic columns appear lighter (even fading away) and the edge irregularities become apparent. Fig. 15 shows experimental images of Pt particles. The effect of fading out at the edges can be clearly observed.

We conclude that all the theoretical and experimental evidence shows that small particles are rough. Most of the work in catalysis on small particles was based on the idea of correlating atomic sites in flat low index surfaces or in corners of regular polyhedral shapes. In the classical work of Van Hardeveld and Hartog [34] the number of

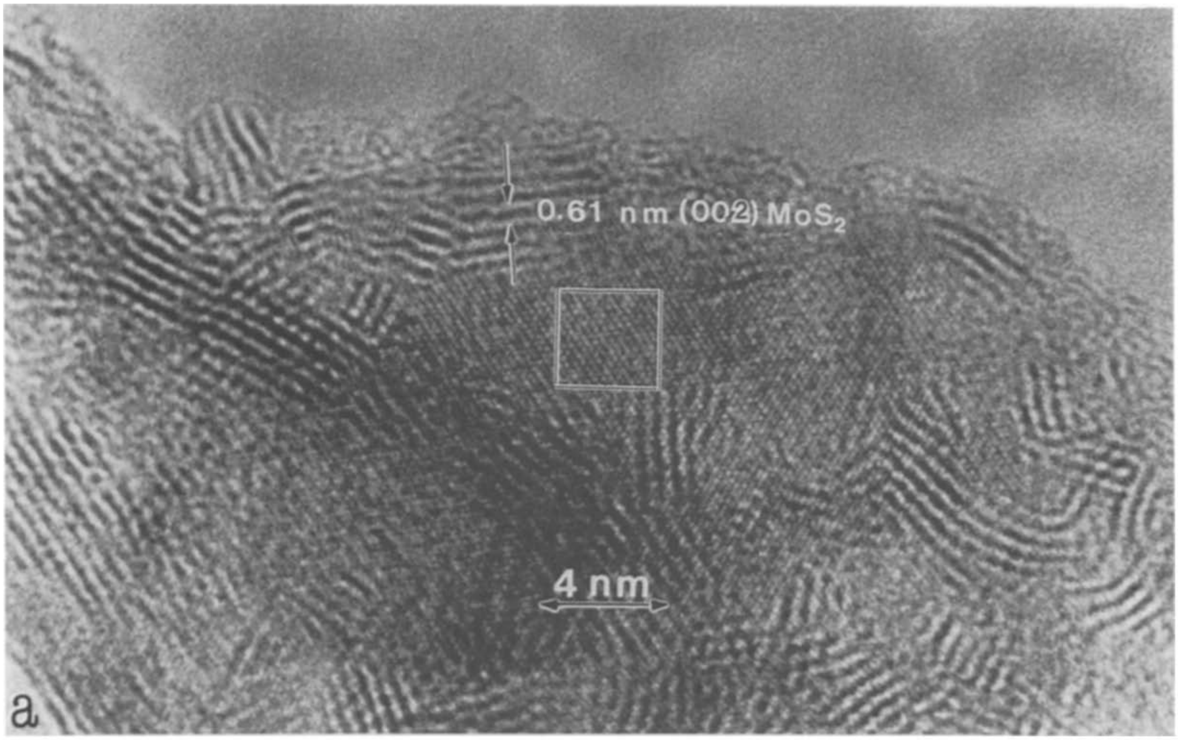

Fig. 22. (a) HREM image of a CoMo sulphide. (b) Reconstructed image of a portion of (a). (c) Theoretical image of $CoS_{1.035}$ along a ⟨011⟩ direction. (d) Comparison of the theoretical and experimental image.

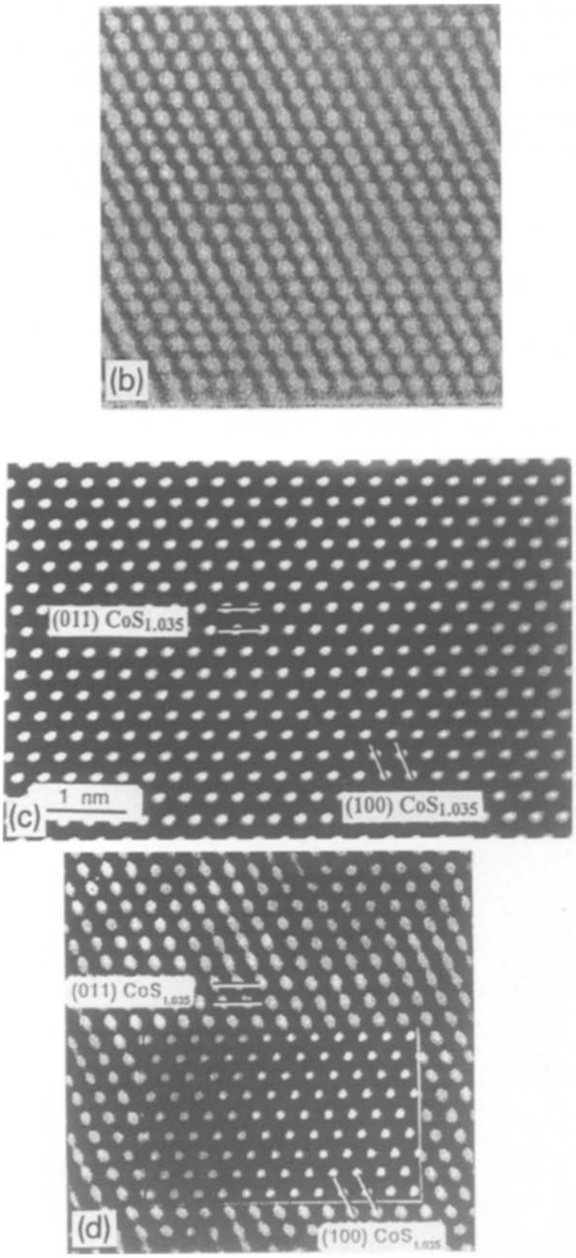

Fig. 22. (continued).

sites of different atomic coordination were counted. In view of our results the nature of the sites is more complex that originally expected. Indeed, it seems that the roughness effect is the dominant factor with the shape and even the crystal structure of the particle being less relevant for catalysis than the surface roughness.

8. Examples of applications of HREM techniques to the characterisation of metallic nanoparticles

8.1. Colloidal particles

Colloidal particles of noble metals can be produced by reduction of their hydrated metal ions. The optimisation of the preparation conditions lead to the interesting possibility of preparing particles with a wide range of sizes and structures [35,36]. This possibility in particular is important to the idea of preparing supported monodispersed catalysts. Particles prepared by colloidal methods tend to form anomalous structures including structures with a five-fold symmetry axis whose properties are unlike those of common metals. As an example, Pd and Pd–Au particles were prepared using this procedure. The morphology of palladium particles prepared by colloidal methods is strongly affected by the nature of the reducing agent. Fig. 16a and b show HREM images of Pd particles obtained using formic acid as reductor [37]. Particles with twinned icosahedral and decahedral structure are evident in this type of preparation. In the case of Pd–Au particles [38], the smaller particles have a rounded profile and the larger ones have faceted shapes. A small particle of about 5.0 nm is shown in Fig. 16c. A single twinned structure is observed.

8.2. Bimetallic catalysts

The behaviour of a metal in a catalytic reaction can be modified by combining it with a second metal which may be either active or inactive for a given reaction. Changes which occur at the metal surface by addition of another metal may be reflected by changes in the selectivity, activity and/or stability of the active phase. The catalytic properties of bimetallic catalysts usually deviate from the additive properties of the individual metals. Electronic or ensemble effects have been invoked in an attempt to explain this behaviour. The characterisation of the phases present in bimetallic systems is consequently of great importance in any attempt to understand the behaviour of a bimetallic catalyst.

The following example concerns the PtNi system for which metastable intermetallic phases have been reported in the bulk. PtNi particles obtained by sputtering techniques and subsequent reduction in hydrogen [39] where characterised using a JEOL 4000EX electron microscope. Fig. 17a shows an original image of a selected zone of the sample. Lattice and atomic resolution allows the measurements of the interplanar distances and it was found to correspond to the NiPt and Ni_3Pt phases. Additional computational work was done in order to verify the presence of the Ni_3Pt phase. Fig. 17b shows the theoretical image of the Ni_3Pt phase calculated using a multislice image simulation. The same image showing the position of the atomic columns of Pt and Ni is presented in Fig. 17c where black dots correspond to the Ni atoms. Fig. 17d shows an amplified image with enhanced contrast of a portion of Fig. 17a. A good agreement between the theoretical and the experimental image is observed leading to an unambiguous characterisation of the Ni_3Pt phase [40]. The

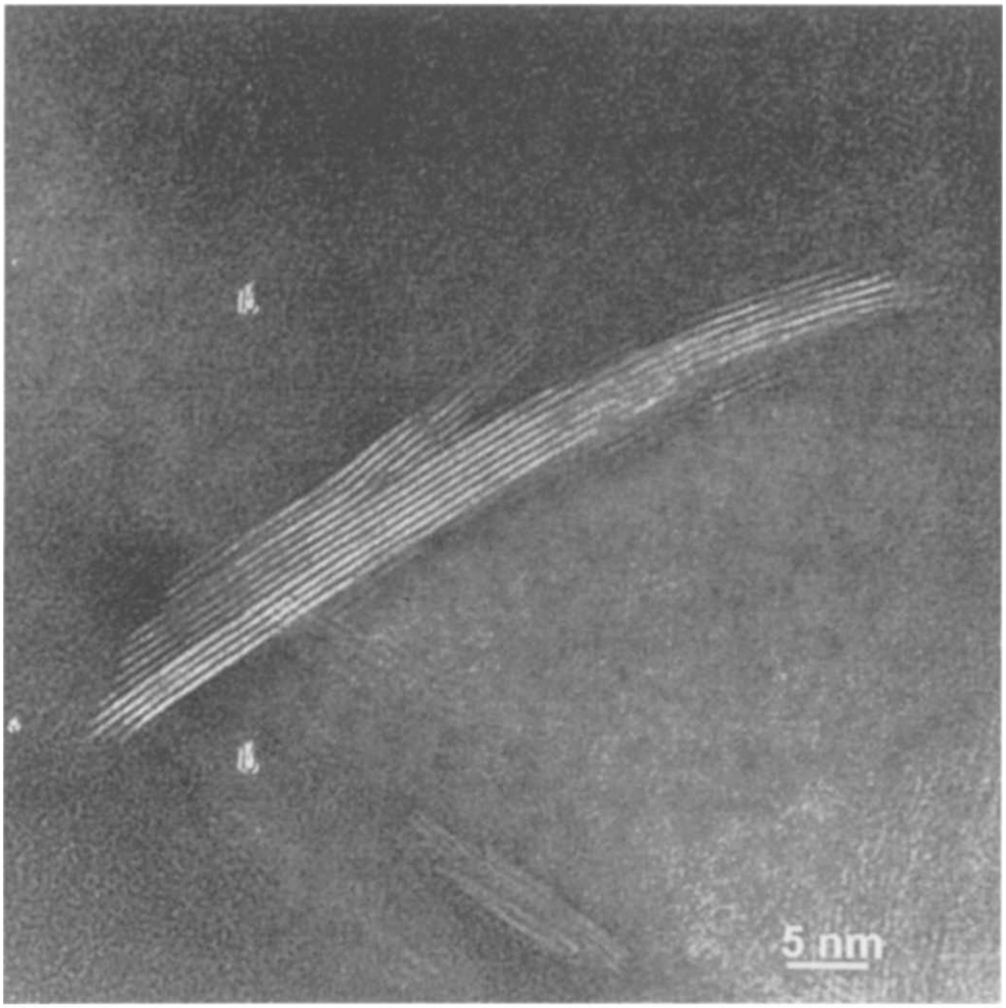

Fig. 23. Experimental HREM image of stacked layers in a MoS_2 catalyst.

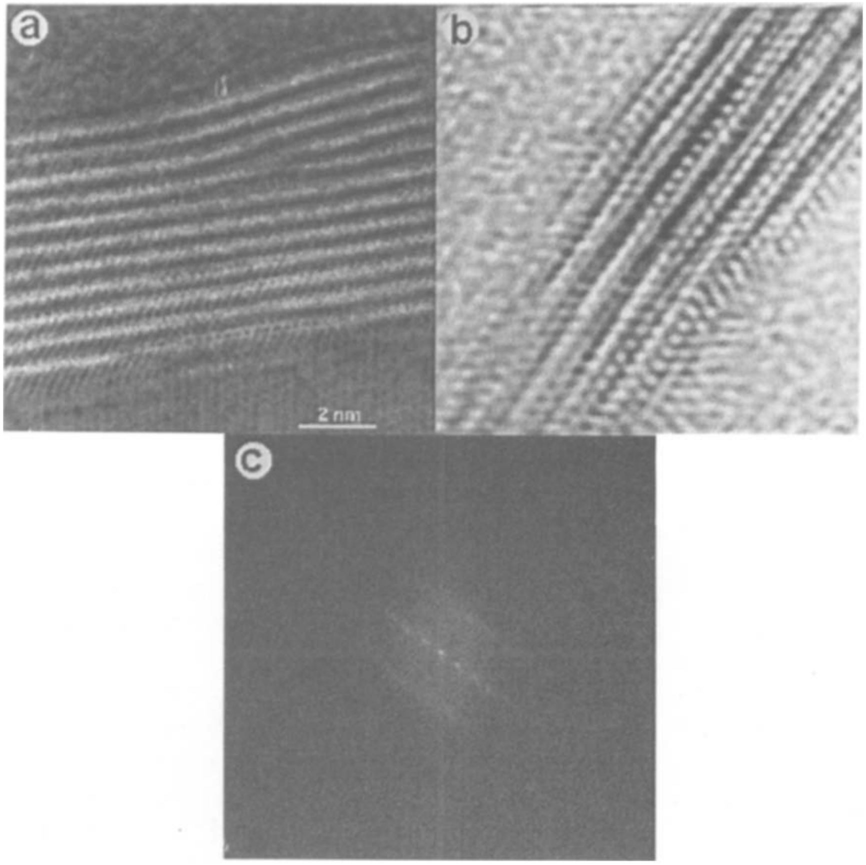

Fig. 24. (a) HREM of stocked layers in a MoS_2 structure showing atomic resolution in two perpendicular directions. (b) Image of MoS_2 along the (110) direction showing the 'spiral-like' array of atoms. (c) Corresponding FFT of the previous picture.

presence of this phase at the nanolevel could have some interesting implications on our understanding of PtNi supported catalysts.

8.3. Pt/Al_2O_3 catalysts

The characterisation of small supported metallic particles is very important in view of their relevance to catalytic problems. HREM has been of importance in elucidating the shape, roughness and surface structure of small particles. Two main approaches have been used in this view: the study of real catalysts and the simulation of the surface of a real catalyst using model catalysts prepared by deposition from the vapour phase onto an inert support. In any case the main goal is to provide information about the microstructure of the particles in an attempt to correlate this information with catalytic properties.

In the following example of characterisation, platinum particles from a Pt/Al_2O_3 catalysts were observed using a JEOL 4000EX microscope and digitised using a CCD device. Fig. 18a shows a selected zone of a Pt/Al_2O_3 catalysts reduced at 400°C in H_2. A faceted Pt particle showing atomic resolution is observed. Fig. 18b shows the FFT of this particle, where the ⟨011⟩ zone axis is recognised [41].

A really amazing feature of this particle is that in spite of its small size ca. 20 Å it has very well defined facets. The crystallinity of the sample is shown by the well defined spots in the FFT.

The well defined and symmetric shape of this particle (obtained by reduction of a metal compound on a support), contrasts with the case of small particles obtained by evaporation of Pt metal as shown in Fig. 19. The differences could be related to the equilibrium state of the particle. In the first method particles have enough time and a high enough temperature to reach well defined and regular shapes. It appears that the particles evaporated on amorphous carbon grown in a way that follows the Sachdev et al. [42] model.

Those model calculations, are made for a free-standing cluster, it seems however, that for the case of real catalysts such as the Pt/Al_20_3, particles have a remarkably well defined shape. This is probably due to the interaction of the particle with the support. In addition it should be said that evaporated particles when they grow and coalesce tend to become more crystalline as shown in Fig. 20.

8.4. *Effects on the catalyst support*

Transition metals are important as catalysts in a large variety of important reactions in the chemical industry, for example in exhaust emission control and gas purification, among others. The active metal component is very often supported on high surface area carriers, e.g. refractory inorganic oxides. Of the most common supports used in designing supported metal catalysts, aluminas and zeolites represent about 80% of all industrial supports. The role of the support in supported metal catalysts can vary. Different metal–support interactions may lead to particles with different morphologies, surface compositions in the case of multimetallics, dispersions, etc. In addition, changes in the substrate during catalysts pretreatments or activation processes may have some influence on these parameters. Fig. 21 shows the effect of a treatment in H_2S/H_2 atmosphere at 400°C during 4 h of a microcrystalline Al_20_3. Fig. 21a and b clearly show a recrystallization of the substrate after this treatment. The direct measurement of the interplanar spacing in Fig. 21b corresponds to the Al_20_3 cubic phase. Nevertheless in Fig. 21a (marked region) it is possible to see interplanar distances and angles which do no match with this phase. This result might be explained by an incomplete crystallization of the Al_20_3 at these experimental conditions or the possibility of a new phase which probably includes sulphur atoms on it. In any case the eventual modification of the substrate crystallinity greatly influences the morphology and structure of the supported metallic particles.

8.5. *Molybdenum sulphide catalysts*

The attainment of knowledge about the structure of promoted molybdenum disulphide based catalysts has been one of the most important objects of research in recent years. Two approaches are currently being used to explain the promoting effects of Co or Ni in MoS_2 catalysts: the electronic model [43] and the geometrical model [44]. In the former an electron transfer from the promoter to molybdenum is involved while in the latter a specific cobalt phase existing only in combination with MoS_2 leads to the observed synergy in this system. The structure of bulk sulphides is dependent on the preparation method HREM of Co–Mo bulk sulphides prepared by HSP and ITD methods have shown structural differences [45]. In addition, the MoS_2–H_2 and Co_9S_8 phases were identified nevertheless, the presence of other cobalt phases (CoS_{1+x}) could not be shown but can not be disregarded.

Fig. 22a shows the HREM image of a CoMo sulphide prepared by impregnated thiosalt decomposition and submitted to a crystallization procedure. After direct measurements of the interplanar distances, the MoS_2 and $CoS_{1.035}$ phases were identified. Fig. 22b shows the reconstructed image of the marked portion of the image in Fig. 22a. The theoretical image of the $CoS_{1.035}$ phase along the $\langle 011 \rangle$ direction, calculated for a sample of 3 nm thickness and a defocus of -40 nm is shown in Fig. 22c. A very good agreement between the theoretical and the experimental filtered image is observed. Fig. 22d shows this comparison. The use of HREM and image simulation techniques has allowed the identification of this cobalt sulphide in samples prepared by the ITD method [46].

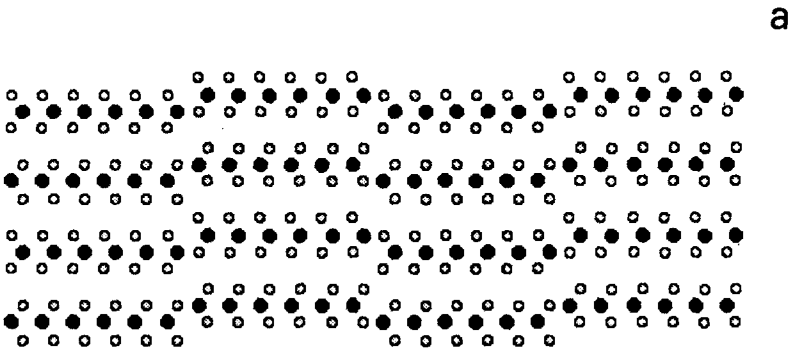

MoS2 DES (100)

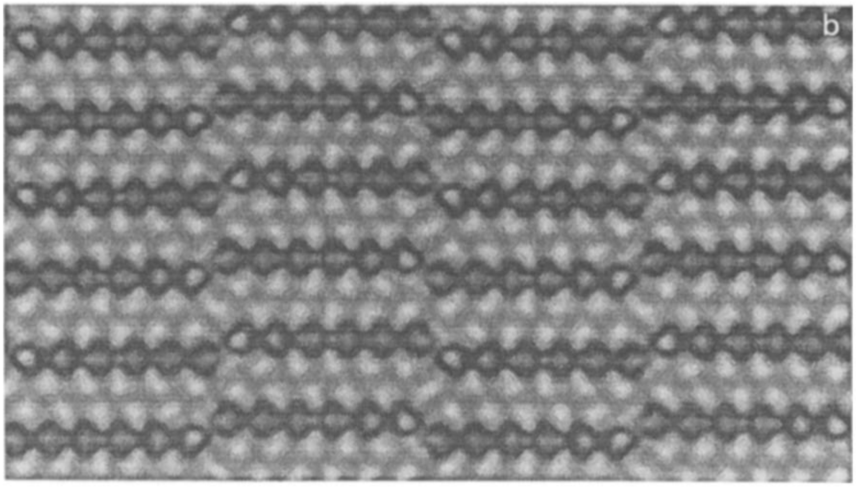

MoS2 DES Z=100 V=400k T=300 Å Df= -200 Å Cs= 1.0mm DEL=80Å DIV=0.6mr R=0.7

Fig. 25. (a) Model of a displacement defect in the ⟨110⟩ direction of a MoS_2 crystal. (b) Image corresponding to the model showing an 'spiral-like' contrast.

8.6. MoS_2-rag-type

As pointed out before MoS_2 catalysts promoted with Co or other metals are very important in several areas of modern catalysis [43]. MoS_2 can be produced in a morphological structure termed 'rag-type' [47]. By varying the conditions of preparation, the number of stacks and the dimensions of the layers can vary. A typical structure is shown in Fig. 23. We can now produce HREM images of the MoS_2 stacked layers. Two images of this kind can be seen in Fig. 24a and b with the corresponding FFT of Fig. 24b shown in Fig. 24c. It should be noted that although pictures of this kind of structure have been published before [48], this is the first time in which atomic resolution is shown along the axis of the fiber and in a perpendicular direction. Atomic lines of 6.2 Å apart have atoms separated by 2.5 Å. A remarkable fact of Fig. 24b is that lines of atoms seem to roll one over the other as if a spiral structure is present. Enormous caution should be taken in interpreting these images. It is well known from the literature that similar (not equal) effects can be produced

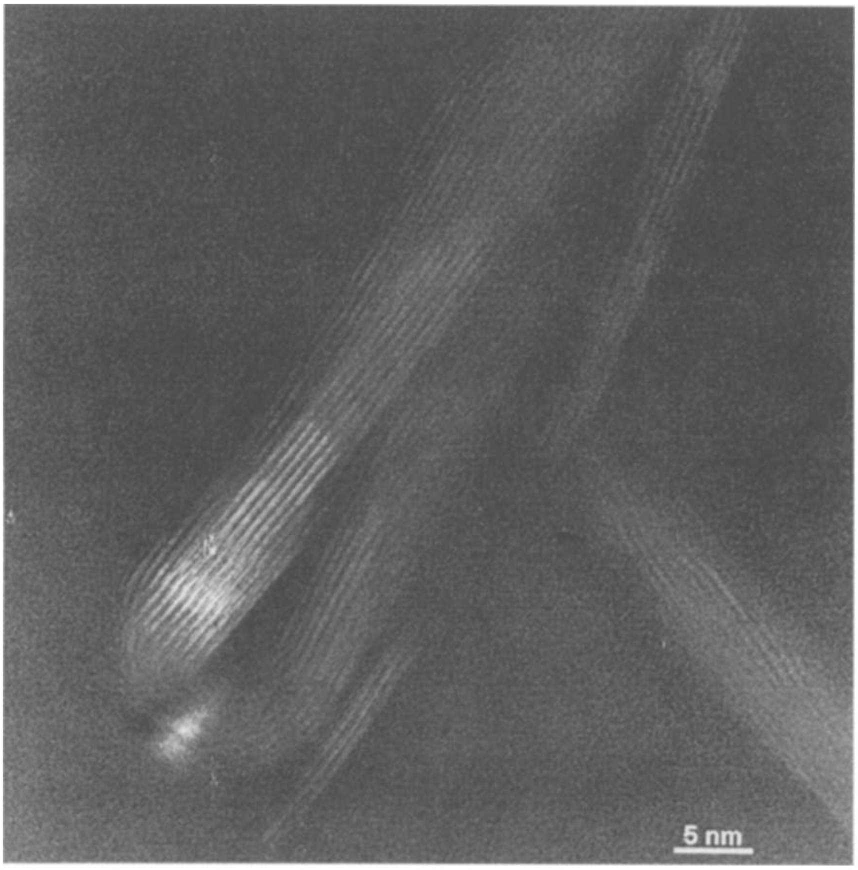

Fig. 26. Image of a folded MoS_2 structure which should contain pentagonal and heptagonal arrays of atoms at the folded tip.

by thickness variations, however we think that in the present pictures this is not the case because the sample is very thin. Computer simulations also show that thickness variations alone do not produce the effect. It is necessary to introduce some kind of defect on the sample to get images, that approach those observed experimentally. An example is shown in Fig. 25 where (a) shows the model of a displacement in the ⟨110⟩ direction and the corresponding simulated image in (b). Although we have not been able to determine the defect that generates the spiralling effect, it is clear that the spiral is not necessary the answer to the structure. Finally another fascinating structure which is produced in MoS_2 is shown in Fig. 26. In this case the structure is folded forming a kind of cage. These structures are similar to the fullerene cages found recently [49,50] and similar cages, not exactly the same as the one shown here, have been reported in sulphides [51]. The folding of structure such as in graphite formed by hexagonal layers implies that heptagonal and pentagonal arrays of atoms are formed as shown by Mackay and Terrones [52]. It is however not trivial to see how these hexagonal arrays are formed in a two atom layered component such as MoS_2. This is one of the most fascinating future points of research into the future of sulphides and bridges two fascinating fields of modern science; catalysts and fullerene science.

9. In-situ studies of particles

High resolution studies can also provided another fundamental window for catalyst studies.

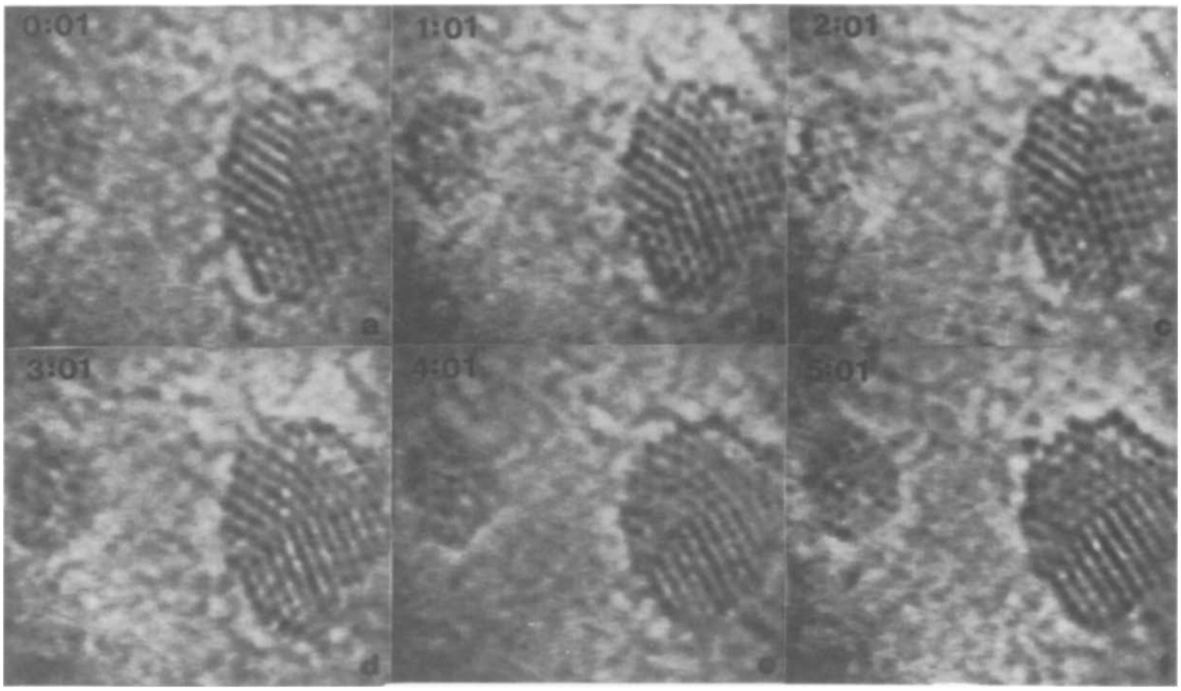

Fig. 27. Sequence of a small particle showing structural transitions. The particle goes from cubo-octahedral to icosahedral going through single twinned and amorphous states.

The in-situ observations allow us to understand some basic kinetic phenomena on crystals. Even if the vacuum of the TEM is not good enough a lot of the basic physics and chemistry of catalysts can be learnt. Classical examples of this are the work of Baker and Harris and Endo et al. [53,54] in the growth of carbon fibers.

We have also studied the dynamic behaviour of nanoparticles using high resolution a TEM JEOL 4000FX instrument fitted with extra vacuum pumps and an evaporation chamber designed by Krakow [55]. The machine is capable of producing a 10^{-8} Pa pressure around the sample. We have studied the growth of gold particles [56] using this machine. An interesting sequence is shown in Fig. 27 and corresponds to an oscillation on the structure of the particle as we observe it. The particle undergoes a transition from cubo-octahedral to icosahedral and back to cubo-octahedral passing through a number of intermediate states such as single twinned and amorphous. This kind of structure oscillation was first discovered by Iijima [57] and Bovin and Melm [58] and was termed quasimelting by Ajayan and Marks [59]. Work, using mid-resolution, by José-Yacamán and Miki-Yoshida [60] indicated that during coalescence the particles tend to undergo quasimelting before actually merging into a single particle. High-resolution studies confirmed this fact [56]. A typical sequence showing this can be seen in Fig. 28. Here the small particles undergo quasimelting before coalescing. The way this phenomenon is induced is not clear. The electron beam might play a significant role. [61]. Other researchers have stated that in any situation in which the particles are free from the substrate, this phenomenon will happen spontaneously [57]. It is clear from theoretical calculations [62] that the particles have several states with a similar energy all contained between the cubo-octahedron and the icosahedron. Therefore under any excitation the particle might jump from one state to another. The activation energy necessary to jump the energy barrier with the substrate can be provided by the energy transferred by the electron beam or by heating. In fact it is very likely that during a

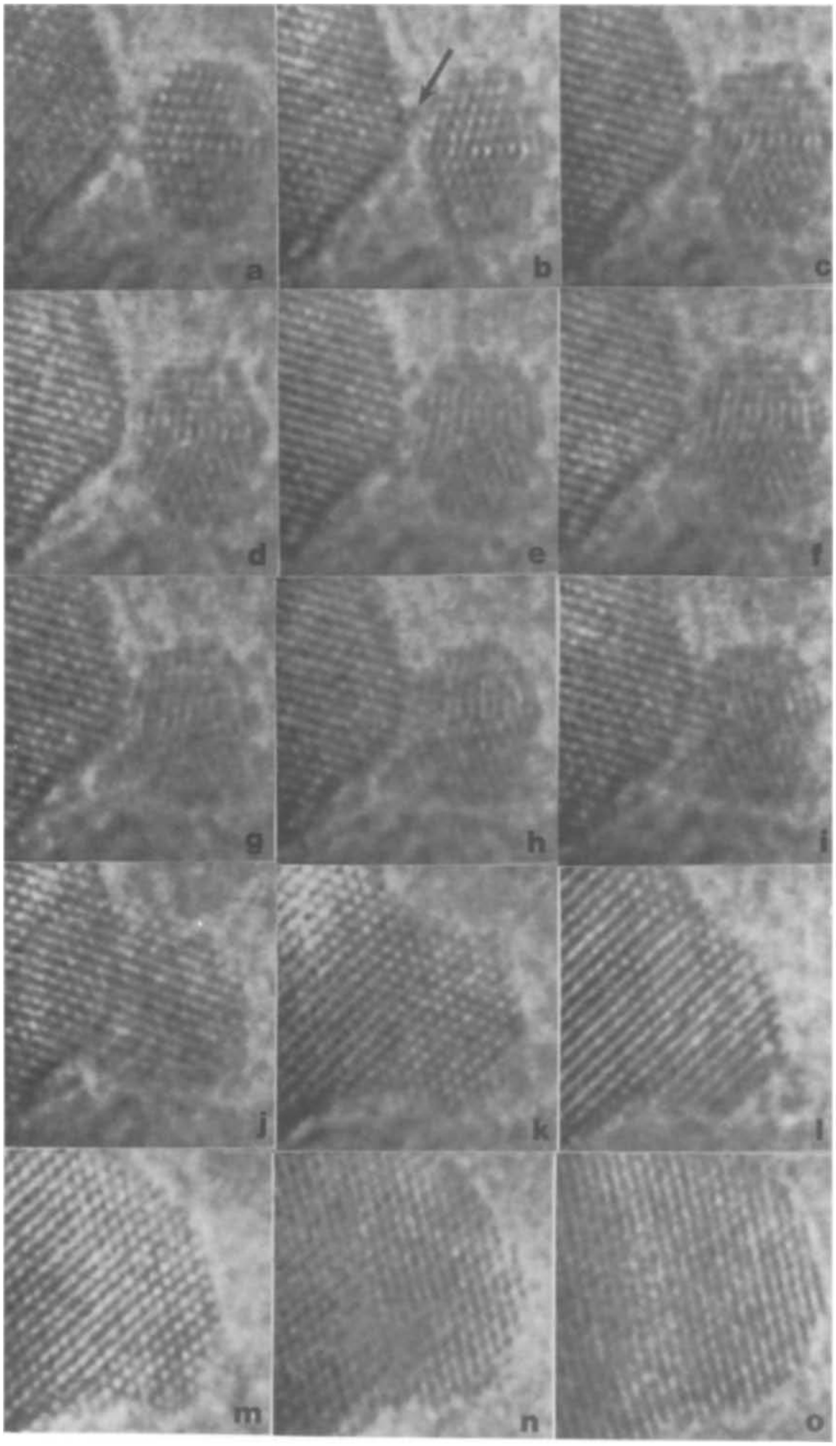

Fig. 28. HREM sequence of two particles in the process of coalescence. Note that the smaller particle undergoes structural changes before coalescence.

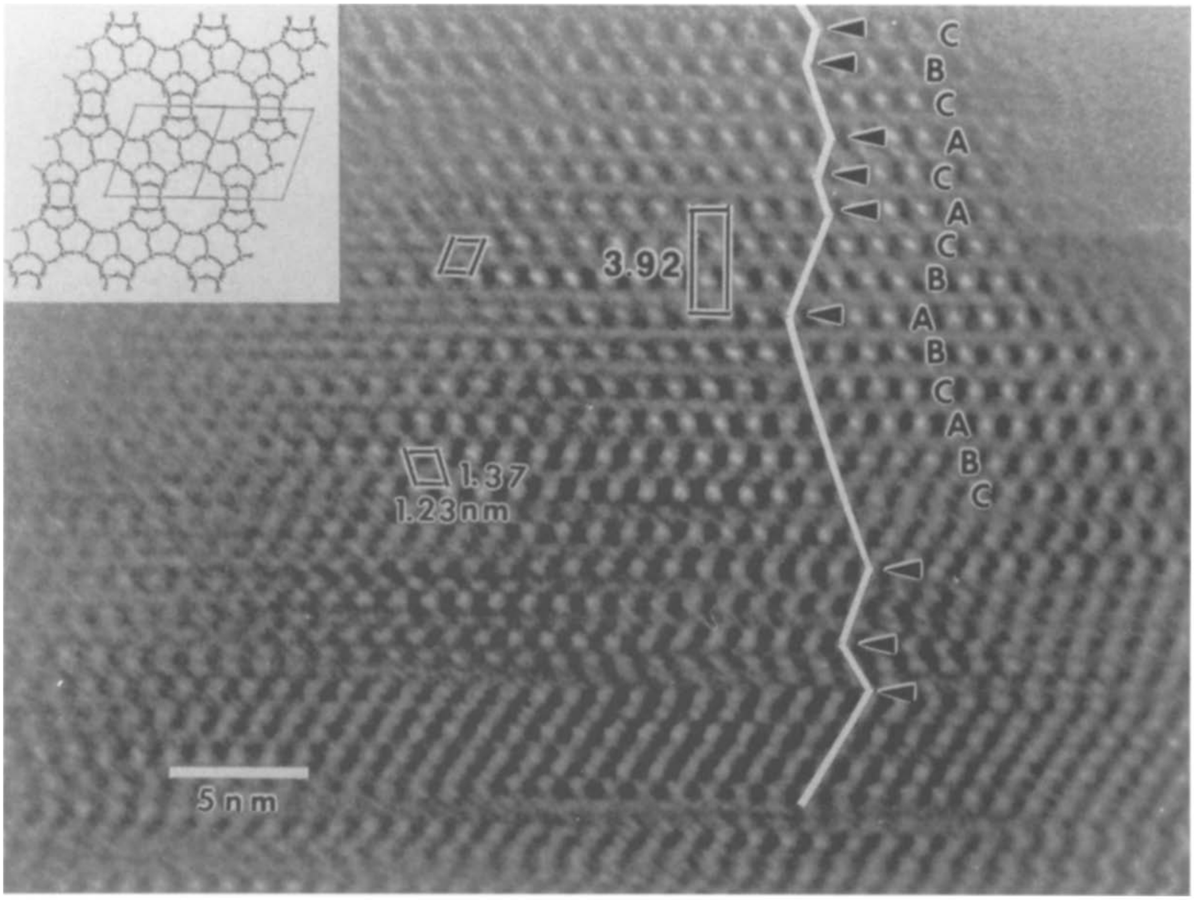

Fig. 29. HREM image of a zeolite beta showing the defects on the structure. The inset shows a theoretical image of the structure.

reaction the particles might start quasimelting due to energy transferred by the reactant species. In any case this will imply that sites on the surface are continuously changing.

10. Other materials

In this section we will present examples of HREM studies of materials such as zeolites and carbon fibers. In the case of zeolitic materials HREM have played an important role.

Zeolite beta is a high-silica zeolite. Structural characterisation of this zeolite using powder X-ray diffraction, HREM and computer assisted modelling has been carried out by Newsam et al. [63]. In an independent study, the lattice parameters of zeolite beta were determined by means of the geometric construction of the reciprocal plane. In order to confirm the structural model HREM images were taken. Fig. 29 shows a HREM image of zeolite beta projected down a ⟨010*t*⟩ axis. The channels of 5-member rings and 5- with 4-member rings together are shown clearly. In the insert a model of the structure accords fairly well with the experimental image. Fig. 29 provides information to explain the indistinct regions of HREM images previously reported [64]. In fact, in zeolite beta there are not only stacking faults in the ⟨001*t*⟩ direction, but also defects in the ⟨100*t*⟩ and ⟨010*t*⟩ directions. Because the atomic displacement of different layers in ⟨100*t*⟩ and ⟨010*t*⟩ directions are different, they destroy the completeness of the crystal lattice and result in indistinct HREM images of ⟨010*t*⟩ orientation, with *t* indicating an arbitrary number.

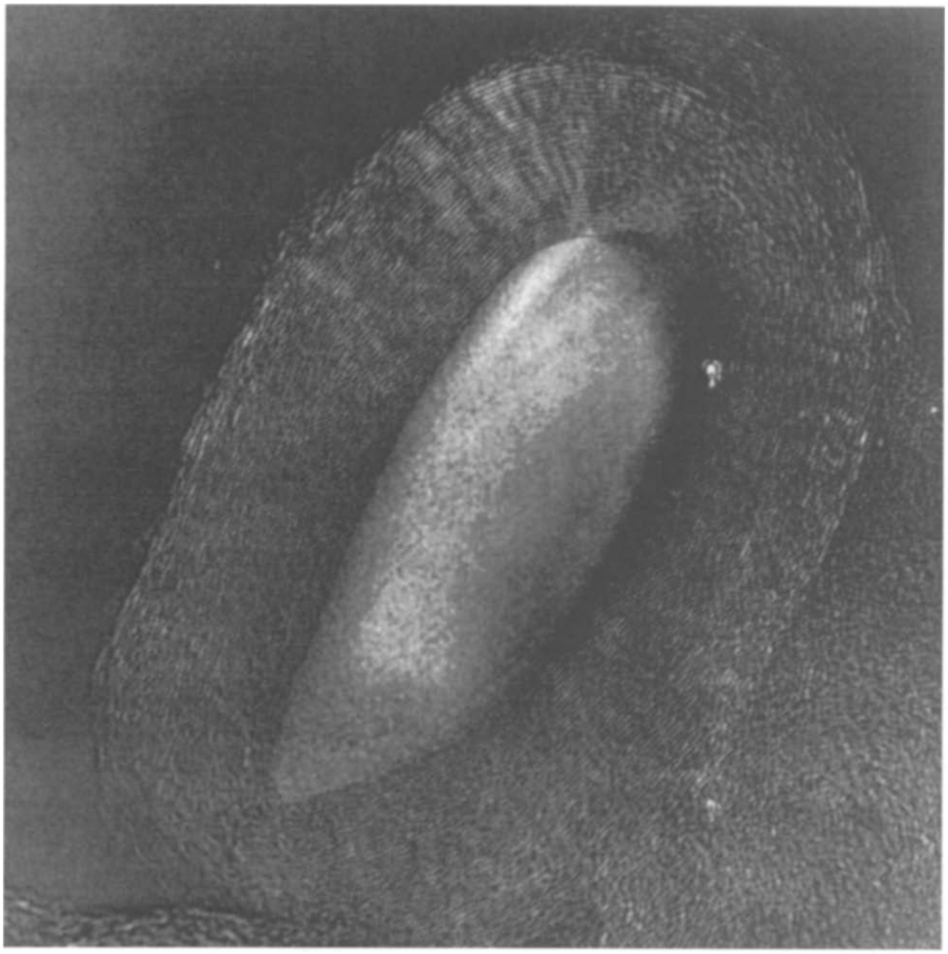

Fig. 30. Image of graphite planes encapsulating a F_3C particle with ellipsoidal shape.

Another extremely interesting case is that of the fullerene materials. The recent discovery of experimental methods to produce C_{60} and higher fullerenes has generated a great deal of research. The formation of carbon filaments from catalytic decomposition of carbon containing gases over metal surfaces has been known for some time [65]. However, it was not recognised that these methods could be used to grow buckytubes, having the advantage of a better control of the dimensions of the microtubules and the possibility of producing macroscopic size fibers. Fig. 30 shows an image of the initial stages of growth of a carbon fiber around a Fe particle in a Fe/C catalyst [66]. These fibers adopt the shape of the metal particle over which it grows. Fig. 30 shows an elliptical particle around which, an elliptical structure of grapheme is nucleated [67]. The particle corresponds to F_3C with (002) atomic planes with an interplanar distance of 1.43 Å.

11. HREM of the future

To close this paper we would like to raise the questions of what can we expect in the future and what are the relevant points that can be developed in a microscope? Recently a new high-voltage microscope of 1250 keV and a resolution ca. 1.0 Å was described [68]. However, the general tendency does not seem to be in the high-voltage direction. The dramatic improvements for the future will come from the use of highly coherent field-emission gun (FEG) sources. This will allow the combination of HREM and chemical analysis at an atomic level. Machines with FEG that achieve an information limit of ca. 1.1 Å and can provide chemical analysis of areas ca. 8 Å are already available on the market. Compared to conventional electron sources the use of highly coherent field emission sources improves the information resolution considerably. However, the retrieval of this extra information is not direct because the phase and amplitude of the electron wave are mixed in a complicated way in the image plane. In order to obtain additional high-resolution interpretable information, it is necessary to use a procedure for phase retrieval. Examples of this method using focal series were shown by Coene et al. [69], or using tilt azimuth series (or a combination of both approaches) by Kirkland et al. [70]. These methods offer great possibilities for the study of nanoparticles in catalysts. An improvement of the interpretable resolution from 2.3 Å to 1.4 Å in gold particles has been demonstrated recently [70].

Probably the most exciting possibility for the future of catalyst studies is that of performing an analysis of nanoareas using EELS (electron energy loss spectroscopy). This will provide a lot of useful information about the detailed chemical composition of nanoparticles. So the microscope of the future would appear to be a medium voltage machine with a field-emission gun, capable of performing EELS that will provide chemical mapping and X-ray analysis, a CCD camera for image acquisition and on-line image processing. Since the future is nearer than it looks, several commercial instruments have already appeared on the market which look very similar to the one we have described. Also some other techniques such as electron loss near edge structure (ELNES) provide information on the bonding and chemical environment of an atom. This technique, difficult to apply to small particles, is likely to have an important impact on the future.

It will also be important in the future to perform more extended calculations on images of nanoparticles. Although some image simulations taking into account a number of effects have been published [71], it is necessary to include the effect of elastic scattering of initially inelastically scattered electrons, true effects of beam divergency and the effect of an incomplete number of unit cells in FCC structures (or in five-fold particles) as pointed out recently by Jefferson [72]. Additionally it will be necessary to obtain better models of particles with structures which are intermediate between FCC and five-fold in order to compare with the experiments.

Computer processing should be an integral part of the microscope. Dramatic improvements on the processing software will be achieved in the next few years. Undoubtedly TEM will continue, in the years to come, to play a fundamental and ever more important role in catalysis research.

Acknowledgements

The authors would like to express their gratitude to all the persons who collaborated on the work presented here. Our thanks particularly go to Samuel Tehuacanero for the image processing work and to Cristina Zorrilla for the computation of images. We would also like to thank Luis Beltrán del Río and Antonio Gómez-Cortés for technical help and Dr. P. Schabes for letting us have his unpublished work. Technical discussions with Armando Vázquez, S. Fuentes, M. Che, W. Krakow and J.L. Aragón are acknowledged. We also thank Dr. Russ Chianelli for suggesting the work on sulphides and for many illuminating discussions. We would also like to recognise the technical work of Luis Rendón who obtained most of the pictures presented in this work.

References

[1] M. Che and C. Bennet, Adv. Catal., 36 (1989) 55.
[2] D.J. Yates and J.H. Sinfelt, J. Catal., 8 (1967) 348.
[3] D.J. Yates, L.C. Murrel and E.B. Prestridge, J. Catal., 57 (1979) 41.

[4] E.B. Prestridge, G.H. Via and J.H. Sinfelt, J. Catal., 50 (1977) 115.

[5] J.V. Sanders, Catalysis, Science and Technol., 7 (1982) 52.

[6] M. José-Yacamán and T. Ocaña, Phys. Status Solidi, A42 (1977) 571.

[7] M. José-Yacamán, in R. Vanselow and R. Howe (Editors), Chemistry and Physics of Solid Surfaces V, CRC Press, Boca Raton, 1984.

[8] J. Shu and J.M. Cowley, Acta Cryst., A38 (1982) 718.

[9] K. Heinemann and H. Poppa, Appl. Phys. Lett., 20 (1972) 122.

[10] M. José-Yacamán and M. Avalos Borja, Catal. Rev. Sci. Eng., 34 (1992) 55.

[11] M. José-Yacamán and J.M. Domínguez, J. Catal., 64 (1980) 223.

[12] M. José-Yacamán, K. Heinemann, Y. Yang and H. Poppa, J. Cryst. Growth, 47 (1979) 187.

[13] M. Gillet, Surf. Sci., 67 (1977) 139.

[14] L.D. Marks and D. Smith, J. Cryst. Growth, 54 (1981) 425.

[15] M. Avalos, F.A. Ponce and K. Heinemann, in F.A. Ponce and M. Cardona (Editors), Proceedings in Physics 62, Surface Science. Lectures on Basic Concepts and Applications, Springer-Verlag, Berlin, 62 (1992) 83.

[16] E. Kirkland, Ultramicroscopy, 15 (1984) 151.

[17] J.C. Spence, Experimental High-Resolution Electron Microscopy. Oxford University Press (1988).

[18] L. Beltrán del Río, A. Gómez and M. José-Yacamán, Ultramicroscopy, 38 (1991) 319.

[19] A. De Jong, W. Coene and D. Van Dyck, Ultramicroscopy, 27 (1989) 53.

[20] J. Song and E.J. Delp. Computer Vision, Graphics, and Image Processing, 50 (1990) 308–328.

[21] A. Beghdadi and A. Le Negrate. Computer Vision, Graphics, and Image Processing, 46 (1989) 162

[22] M.I. Sezan, Computer Vision, Graphics, and Image Processing, 49 (1990) 36.

[23] J. Otsu, IEEE Trans. on Systems, Man, and Cybernetics, 9 (1979) 1.

[24] F.M. Mulder, T.A. Stegink, R.C. Thiel, L.J. de Jongh and G. Schmid, Nature, 367 (1994) 716.

[25] R. Herrera, PhD Thesis, CICESE Ensenada (1985).

[26] P.A. Stadelmann, Ultramicroscopy, 21 (1987) 131.

[27] M. Fluei, PhD Thesis No. 796 EPFL, Lausanne (1989).

[28] M. José-Yacamán and M. Avalos, Ultramicroscopy, 10 (1983) 211.

[29] M.H. Yao and D.J. Smith, J. Microscopy., 175 (1994) 252.

[30] M. José-Yacamán, P. Schabes, R. Herrera, A. Gómez and S. Tehuacanero, Surf. Sci., 237 (1990) 248.

[31] L.M. Beltrán del Río, A. Gómez and M. José, in B. Jouffrey and C. Colliex (Editors), Proceedings of ICEM-13, Vol. 1, 1994, p. 443.

[32] S. Pacionik, R. Kilaas, U. Dahmen and M. O'Keefe, in G.W. Bailey and C.L. Riedel (Editors), Proceedings of 51st Annual EMSA Meeting, San Francisco Press, San Francisco, 1993, p. 458,

[33] W.O. Saxton and D.J. Smith, Ultramicroscopy, 18 (1985) 39.

[34] R. Van Hardeveld and F. Hartog, Surface Sci., 15 (1969) 189.

[35] J. Turkevich and G. Kim, Science, 169 (1970) 875.

[36] P. Sermon, K. Keryou, J.M. Thomas and C.R. Millward, Mat. Res. Symp., Series III, 1988, p. 13.

[37] G. Díaz, M. Viniegra and M. José-Yacamán, Actas XIII Congr. Iberoam. Catal., II, 1992, p. 971.

[38] R. Hernández, A. Vázquez, G. Díaz, M. Avalos and M. José-Yacamán, Mat. Res. Soc. Symp. Proc., 177 (1990) 231.

[39] J.A. Arenas Alatorre and P.S. Schabes Retchkiman, presented at 2nd Interamerican Congress on Electron Microscopy (1993).

[40] J.A. Arenas Alatorre and P.S. Schabes Retchkiman, Proceedings 13th International Congress on Electron Microscopy (1994).

[41] M. José-Yacamán, R. Herrera, S. Tehuacanero, A. Gómez and L. Beltrán del Río, Ultramicroscopy, 33 (1990) 133.

[42] A. Sachdev, R.I. Masel and J.B. Adams, J. Catal., 136 (1992) 320.

[43] S. Harris and R.R. Chianelli, J. Catal., 98 (1986) 17.

[44] (a) H. Topsoe, B.S. Clausen, R. Candia, C. Wivel and S. Morup, J. Catal., 68 (1981) 433. (b) M. Ledoux, O. Michaux, G. Agostini and P. Panisso, J. Catal., 96 (1985) 189.

[45] J. Cruz-Reyes, M. Avalos-Borja, M.H. Farias and S. Fuentes, J. Catal., 137 (1992) 232.

[46] G. Díaz, R. Luna, D. Ríos-Jara, L. Baños and M. Avalos-Borja, submitted to J. Mol. Catal.

[47] R.R. Chianelli, E.B. Prestridge, T.A. Pecoraro and J.P. de Neuville, Science, 203 (1979) 1105.

[48] J.M. Thomas, Phil. Tras. Roy. Soc., A277 (1974) 251.

[49] S. Iijima, Nature, 354 (1991) 56.

[50] D. Ugarte, Nature, 359 (1992) 707.

[51] R. Tenne, L. Margulis, M. Genut and G. Hodes, Nature, 360 (1993) 444.

[52] A.L. Mackay and H. Terrones, Phil. Trans. Roy. Soc. London, A343 (1993) 113.

[53] R.T. Baker and P.S. Harris in P.L. Walker and P.A. Thrower (Editors), Chemistry and Physics of Carbon, Marcel Dekker, New York.

[54] M. Endo, T. Koyama and Y. Hishiyama, Jpn. J. Appl. Phys., 15 (1976) 2073.

[55] W. Krakow, personal communication.

[56] W. Krakow, M. José-Yacamán and J.L. Aragón, Phys. Rev. Lett., 49 (1994) 10591.

[57] S. Iijima, Adv. Mat. J. Electron Microsc., 34 (1985) 249.

[58] J.O. Bovin and J.O. Melm, Z. Phys. D, 19 (1991) 293.

[59] P.M. Ajayan and L. Marks, Phys. Rev. Lett., 60 (1988) 585.

[60] M. José-Yacamán and M. Miki-Yoshida, Phys. Rev. B, 46 (1992) 1198.

[61] S Iijima and T. Ichihasi, Jpn. J. Appl. Phys., 24 (1985) L175.

[62] S. Nara, Phys. Status Solidi, B, 149 (1988) 555.

[63] J.S. Newsam, M.M.J. Treacy, W.T. Kotsier and G.B. de Gruyter, Proc. R. Soc. London, A420 (1988) 375.

[64] B.S. Zou, L. Rendón and M. José-Yacamán, submitted to Zeolites.

[65] P.L. Jr. Walker, J.F. Rakszawski and G.R. Imperial, J. Phys. Chem., 63 (1959) 133.

[66] M. José-Yacamán, M. Miki-Yoshida, L. Rendón and J.G. Santiesteban, Appl. Phys. Lett., 62 (1993) 202.

[67] M. Miki-Yoshida, R. Castillo, S. Ramos, L. Rendón, S. Tehuacanero, B.S. Zou and M. José-Yacamán, Carbon, 32 231 (1994) 189.

[68] F. Phillip, R. Möschen, M. Osaki and M. Rübl, Proceedings of ICEM-13, Paris, Vol. 1, 1994, p. 231.